RELAMPAGO-CACTI DROP SIZE DISTRIBUTION OBSERVATIONS AND THE IMPLICATIONS FOR CLOUD AND HYDROLOGIC STUDIES

BY

LINA ESTHER RIVELLI ZEA

THESIS

Submitted in partial fulfillment of the requirements
for the degree of Master of Science in Atmospheric Sciences
in the Graduate College of the
University of Illinois at Urbana-Champaign, 2020

Urbana, Illinois

Advisor:

Professor Stephen W. Nesbitt

Abstract

Comparisons of drop size distributions (DSD) properties and rainfall modes among three deep convective regions (the U.S. Southern Great Plains, in Córdoba Province in subtropical South America, and Manacapuru in central Amazonia) where heavy rain-producing systems contribute the majority of rainfall in the largest river basins of the Americas, are conducted. Measurements from two types of disdrometers sampled at two of the three sites were considered, and subsequently separated into a light precipitation mode and a precipitation mode using a cutoff at 0.5 mm hr^{-1}. The distributions of physical parameters (such as rain rate R, mass-weighted mean diameter D_m, and normalized droplet concentration N_w) for the raindrop spectra without classification appear to be similar amongst the sites, except for much broader distributions of N_w at the Córdoba site. In the light precipitation and precipitation modes, the dominant higher observed frequency of N_w in both types of disdrometers, as well as the identification of shallow, light precipitation in vertically-pointing cloud radar data represent a unique characteristic of the Córdoba site relative to the other sites. As a result, the co-variability between DSD physical parameters indicates that the precipitation observed at Córdoba may confound existing drop size distribution methods of determining rain type.

Acknowledgments

I wish to thank the National Science Foundation grant AGS-1661799, the Department of Energy Atmospheric Systems Research subcontract 408988 from Pacific Northwest National Laboratory, and BECAL Paraguay contract 153/2017 for the financial support for this research. I am also grateful to my advisor Professor Steve Nesbitt for all the feedback over the past years, always having an open door, and for being so active in my research. Also in the University of Illinois Department of Atmospheric Sciences, thank you to Randy Chase, Itinderjot Singh, and Piyush Garg for the fruitful scientific discussions. I thank the RELAMPAGO-CACTI Science Team for the guidance, discussions, and amazing collaboration during the intensive observing period in Córdoba, Argentina.

I am grateful to my colleagues, professors, and the staff from the Department of Atmospheric Sciences at the U of I for sharing their friendship while communicating science.

THANKS Vilma, Chacho, José, Guisella, Sofia, beloved husband Prateek, family and friends for all your support during my journey in Urbana-Champaign.

$VSSVM$.

Table of Contents

List of Tables . . . . . **v**

List of Figures . . . . . **vi**

List of Abbreviations . . . . . **x**

Chapter 1 Introduction **1**

Chapter 2 Data and Methods **6**
2.1 Location of sites 6
2.2 Disdrometer instrumentation 7

Chapter 3 Results **11**
3.1 DSD parameter statistical comparisons 11
3.2 DSDs comparisons in terms of joint 2D-histograms 18
3.3 Comparisons in terms of the DSD shape parameters 23

Chapter 4 Discussion **32**

Chapter 5 Summary and Conclusions **34**

References **36**

List of Tables

2.1 Summary of the disdrometer datasets compiled for this study. 9

3.1 Overview of the correlation between the radar reflectivity factor Z and the mean mass diameter D_m observed in $Lpm - Pm$ and Pm. Power-law curves give by equations from $WL14$ = Williams et al. (Williams et al., 2014); PARS = parsivel disdrometer data, and the 2DVD = two-dimensional video disdrometer data. 25

3.2 Overview of the correlation between the rain rate (R) as 10 log_{10} R and the mean mass diameter as D_m, observed in $Lpm - Pm$ and Pm. Power-law curves give by equations from $WL14$ = Williams et al. (2014); PARS = parsivel disdrometer data, and the 2DVD = two-dimensional video disdrometer data. 25

3.3 Overview of the correlation between the width mass spectrum σ_M and the mean mass diameter D_m observed in $Lpm - Pm$ and Pm. Power-law curves give by equations from $WL14$ = Williams et al. (Williams et al., 2014); PARS = parsivel disdrometer data, and the 2DVD = two-dimensional video disdrometer data. 26

4.1 Overview of the dataset characteristics and pdf peaks from the DSD parameters observed in Lpm and Pm. Multiple peaks were determined subjectively. 33

List of Figures

2.1 Three sites in the largest basins of the Americas with ARM observation available at SGP represents the Southern Great Plains site in Central Oklahoma, U.S. (2017-2019); MAN is the site of the GoAmazon experiment in Manacapuru, Brazil (2014-2015), and COR depicts the site of the CACTI experiment in Villa Yacanto, Argentina (2018-2019). SGP is in a grassland region in the mid latitudes within the Mississippi Basin (red region); MAN is in a region of tropical rain forest or the in tropics within the Amazon Basin (green region), and COR is in a region of complex terrain near the Sierras de Córdoba (SDC) in the mid latitudes within the La Plata Basin (cyan region). 10

3.1 Rain rate (R) as 10 log_{10} R pdfs for DSDs without classification at COR (PARS/2DVD in light blue/blue lines); SGP (PARS/2DVD in dark red/orange lines), and MAN (PARS in green lines). DSDs = raindrop size distributions; PARS = second generation parsivel disdrometer, 2DVD = two-dimensional video disdrometer; COR = Córdoba; SGP = Southern Great Plains, and MAN = Manacapuru. 12

3.2 Rain rate (R) as 10 log_{10} R pdfs for DSDs classified into the light precipitation mode (Lpm : R < 0.5 mm h^{-1}) in dashed lines, and precipitation mode (Pm : R > 0.5 mm h^{-1}) in solid lines; at COR (PARS/2DVD in light blue/blue lines). DSDs = raindrop size distributions; PARS = second generation parsivel disdrometer, 2DVD = two-dimensional video disdrometer, and COR = Córdoba. 12

3.3 Rain rate (R) as 10 log_{10} R pdfs for DSDs classified into the light precipitation mode (Lpm : R < 0.5 mm h^{-1}) in dashed lines, and precipitation mode (Pm : R > 0.5 mm h^{-1}) in solid lines; at SGP (PARS/2DVD in dark red/orange lines). DSDs = raindrop size distributions; PARS = second generation parsivel disdrometer, 2DVD = two-dimensional video disdrometer, and SGP = Southern Great Plains. 13

3.4 Rain rate (R) as 10 log_{10} R pdfs for DSDs classified into the light precipitation mode (Lpm : R < 0.5 mm h^{-1}) in dashed lines, and precipitation mode (Pm : R > 0.5 mm h^{-1}) in solid lines; at SGP (PARS/2DVD in dark red/orange lines). DSDs = raindrop size distributions; PARS = second generation parsivel disdrometer, 2DVD = two-dimensional video disdrometer, and and MAN = Manacapuru. 13

3.5 Mass-weighted mean diameter (D_m) pdfs for DSDs without classification at COR (PARS/2DVD in light blue/blue lines); SGP (PARS/2DVD in dark red/orange lines), and MAN (PARS in green lines). DSDs = raindrop size distributions; PARS = second generation parsivel disdrometer, 2DVD = two-dimensional video disdrometer; COR = Córdoba; SGP = Southern Great Plains, and MAN = Manacapuru. 14

3.6 Mass-weighted mean diameter (D_m) pdfs for DSDs classified into the light precipitation mode (Lpm : R < 0.5 mm h^{-1}) in dashed lines, and precipitation mode (Pm : R > 0.5 mm h^{-1}) in solid lines; at COR (PARS/2DVD in light blue/blue lines). DSDs = raindrop size distributions; PARS = second generation parsivel disdrometer, 2DVD = two-dimensional video disdrometer, and COR = Córdoba. 15

3.7 Mass-weighted mean diameter (D_m) pdfs for DSDs classified into the light precipitation mode (Lpm : R $<$ 0.5 mm h^{-1}) in dashed lines, and precipitation mode (Pm : R $>$ 0.5 mm h^{-1}) in solid lines; at SGP (PARS/2DVD in dark red/orange lines). DSDs = raindrop size distributions; PARS = second generation parsivel disdrometer, 2DVD = two-dimensional video disdrometer, and SGP = Southern Great Plains. 15
3.8 Rain rate (R) as 10 log_{10} R pdfs for DSDs classified into the light precipitation mode (Lpm : R $<$ 0.5 mm h^{-1}) in dashed lines, and precipitation mode (Pm : R $>$ 0.5 mm h^{-1}) in solid lines; at SGP (PARS/2DVD in dark red/orange lines). DSDs = raindrop size distributions; PARS = second generation parsivel disdrometer, 2DVD = two-dimensional video disdrometer, and and MAN = Manacapuru. 16
3.9 Density curves with histograms of the maximum diameter (D_{max}): DSDs in the light precipitation mode (Lpm : R $<$ 0.5 mm h^{-1}) for the PARS at (a) COR, SGP, and MAN sites. DSDs = raindrop size distributions; PARS = second generation disdrometer; COR = Córdoba; SGP = Southern Great Plains, and MAN = Manacapuru. 16
3.10 Density curves with histograms of the maximum diameter (D_{max}): DSDs in the light precipitation mode (Lpm : R $<$ 0.5 mm h^{-1}) for the 2DVD at (a) COR, SGP, and MAN sites. DSDs = raindrop size distributions; 2DVD = two-dimensional video disdrometer; COR = Córdoba; SGP = Southern Great Plains, and MAN = Manacapuru. 17
3.11 Density curves with histograms of the maximum diameter (D_{max}): DSDs in the precipitation mode (Pm : R $>$ 0.5 mm h^{-1}) for the PARS at (a) COR, SGP, and MAN sites. DSDs = raindrop size distributions; PARS = second generation disdrometer; COR = Córdoba; SGP = Southern Great Plains, and MAN = Manacapuru. 17
3.12 Density curves with histograms of the maximum diameter (D_{max}): DSDs in the precipitation mode (Pm : R $>$ 0.5 mm h^{-1}) for the PARS at (a) COR, SGP, and MAN sites. DSDs = raindrop size distributions; 2DVD = two-dimensional video disdrometer; COR = Córdoba; SGP = Southern Great Plains, and MAN = Manacapuru. 18
3.13 Normalized droplet concentration (N_w) as log_{10} N_w pdfs for DSDs without classification at COR (PARS/2DVD in light blue/blue lines); SGP (PARS/2DVD in dark red/orange lines), and MAN (PARS in green lines). DSDs = raindrop size distributions; PARS = second generation parsivel disdrometer, 2DVD = two-dimensional video disdrometer; COR = Córdoba; SGP = Southern Great Plains, and MAN = Manacapuru. 19
3.14 Normalized droplet concentration (N_w) as log_{10} N_w pdfs for DSDs classified into the light precipitation mode (Lpm : R ¡ 0.5 mm h^{-1}) in dashed lines, and precipitation mode (Pm : R $>$ 0.5 mm h^{-1}) in solid lines; at COR (PARS/2DVD in light blue/blue lines). DSDs = raindrop size distributions; PARS = second generation parsivel disdrometer, 2DVD = two-dimensional video disdrometer, and COR = Córdoba. 19
3.15 Normalized droplet concentration (N_w) as log_{10} N_w pdfs for DSDs classified into the light precipitation mode (Lpm : R $<$ 0.5 mm h^{-1}) in dashed lines, and precipitation mode (Pm : R $>$ 0.5 mm h^{-1}) in solid lines; at SGP (PARS/2DVD in dark red/orange lines). DSDs = raindrop size distributions; PARS = second generation parsivel disdrometer, 2DVD = two-dimensional video disdrometer, and SGP = Southern Great Plains. 20
3.16 Normalized droplet concentration (N_w) as log_{10} N_w pdfs classified into the light precipitation mode (Lpm : R $<$ 0.5 mm h^{-1}) in dashed lines, and precipitation mode (Pm : R $>$ 0.5 mm h^{-1}) in solid lines; at SGP (PARS/2DVD in dark red/orange lines). DSDs = raindrop size distributions; PARS = second generation parsivel disdrometer, 2DVD = two-dimensional video disdrometer, and and MAN = Manacapuru. 20
3.17 Two-dimensional frequency histograms for the normalized droplet concentration (log_{10} N_w) and mean raindrop diameter (D_0) in the light precipitation mode (Lpm) R ¡ 0.5 mm h^{-1} at (a) COR, (b) SGP, and (c) MAN sites. DSDs indicated by color contours for the PARS and color-dashed contours for the 2DVD. Lines from $BR09$ (solid green) and $TH15$ (dashed red) for convective-stratiform segregation. 22

3.18 Two-dimensional frequency histograms for the normalized droplet concentration ($log_{10}\ N_w$) versus mean raindrop diameter (D_0) in the precipitation mode (Pm) R > 0.5 mm h^{-1} at (a) COR, (b) SGP, and (c) MAN sites. DSDs indicated by color contours for the PARS and color-dashed contours for the 2DVD. Lines from $BR09$ (solid green) and $TH15$ (dashed red) for convective-stratiform segregation. 22
3.19 Two-dimensional frequency histograms for the liquid water content (LWC) as $log_{10}\ LWC$ versus mean raindrop diameter as $log_{10}\ D_0$ in the light precipitation mode (Lpm) R < 0.5 mm h^{-1} at (a) COR, (b) SGP, and (c) MAN sites. DSDs indicated by color contours for the PARS and color-dashed contours for the 2DVD. Lines from $TH15$ (dashed gray) for convective-stratiform segregation. 22
3.20 Two-dimensional frequency histograms for the liquid water content (LWC) as $log_{10}\ LWC$ versus mean raindrop diameter as $log_{10}\ D_0$ in the precipitation mode (Pm) R > 0.5 mm h^{-1} at (a) COR, (b) SGP, and (c) MAN sites. DSDs indicated by color contours for the PARS and color-dashed contours for the 2DVD. Lines from $TH15$ (dashed gray) for convective-stratiform segregation. 24
3.21 (a) ARM KAZR cloud radar radar reflectivity time-height scans over the COR site during CACTI, collocated with (b) DSD parameter calculations using PARS disdrometer data from 1800 UTC 27 Nov to 0600 UTC 28 Nov 2018. 24
3.22 As in Figure 3.21, but for the period 0000 UTC 23 Feb - 0000 UTC 24 Feb 2019. 26
3.23 Correlation between the radar reflectivity factor Z and the mean mass diameter D_m, in the light precipitation-precipitation mode ($Lpm - Pm$ for each 1-min DSD with at least 50 drops in 5-min consecutive R ¿ 0.10 mm h^{-1}, 0.30 < D_0 < 4.75 mm and Z > 10 dBZ) at (a) COR, (b) SGP, and (c) MAN, and in the precipitation mode (Pm for each 1-min DSD with at least 50 drops in 5-min consecutive R > 0.50 mm h^{-1}, 0.50 < D_0 < 9.50 mm and Z > 10 dBZ) at (d) COR, (e) SGP, and (f) MAN sites. DSDs indicated by color contours for the PARS and color-dashed contours for the 2DVD. Solid lines from $WL14$ (green), $PARS$ (red), and $2DVD$ (cyan) are the Z vs. D_m power-law correlation curves. DSDs = raindrop size distributions; PARS = second generation parsivel disdrometer, 2DVD = two-dimensional video disdrometer; COR = Córdoba; SGP = Southern Great Plains, and MAN = Manacapuru. 27
3.24 Correlation between the rain rate R as $log_{10}\ R$ and the mean mass diameter as D_m, in the light precipitation-precipitation mode ($Lpm - Pm$ for each 1-min DSD with at least 50 drops in 5-min consecutive R > 0.10 mm h^{-1}, 0.30 < D_0 < 4.75 mm and Z > 10 dBZ) at (a) COR, (b) SGP, and (c) MAN, and in the precipitation mode (Pm for each 1-min DSD with at least 50 drops in 5-min consecutive R > 0.50 mm h^{-1}, 0.50 < D_0 < 9.50 mm and Z > 10 dBZ) at (d) COR, (e) SGP, and (f) MAN sites. DSDs indicated by color contours for the PARS and color-dashed contours for the 2DVD. Solid lines from $WL14$ (green), $PARS$ (red), and $2DVD$ (cyan) are the R vs. D_m power-law correlation curves. DSDs = raindrop size distributions; PARS = second generation parsivel disdrometer, 2DVD = two-dimensional video disdrometer; COR = Córdoba; SGP = Southern Great Plains, and MAN = Manacapuru. 28
3.25 Correlation between the width mass spectrum σ_M and the mean mass diameter as D_m, in the light precipitation-precipitation mode ($Lpm - Pm$ for each 1-min DSD with at least 50 drops in 5-min consecutive R > 0.10 mm h^{-1}, 0.30 < D_0 < 4.75 mm and Z > 10 dBZ at (a) COR, (b) SGP, and (c) MAN, and in the precipitation mode (Pm for each 1-min DSD with at least 50 drops in 5-min consecutive R > 0.50 mm h^{-1}, 0.50 < D_0 < 9.50 mm and Z > 10 dBZ) at (d) COR, (e) SGP, and (f) MAN sites. DSDs indicated by color contours for the PARS and color-dashed contours for the 2DVD. Solid lines from $WL14$ (green), $PARS$ (red), and $2DVD$ (cyan) are the σ_M vs. D_m power-law correlation curves. DSDs = raindrop size distributions; PARS = second generation parsivel disdrometer, 2DVD = two-dimensional video disdrometer; COR = Córdoba; SGP = Southern Great Plains, and MAN = Manacapuru. 29

3.26 Box-and-whisker plots for the ratio of maximum raindrop diameter (D_{max}) and mass-weighted mean diameter (D_m): DSDs in the light precipitation mode (Lpm : R < 0.5 mm h^{-1}) for the PARS and 2DVD at COR, SGP, and MAN sites. Tops and bottoms of boxes in blue solid line represent the 75th and 25th quartiles, respectively, and the horizontal red solid lines inside the boxes represent the median. PARS = second generation disdrometer, 2DVD = two-dimensional video disdrometer, COR = Córdoba; SGP = Southern Great Plains, and MAN = Manacapuru. 30
3.27 Box-and-whisker plots for the ratio of maximum raindrop diameter (D_{max}) and mass-weighted mean diameter (D_m): DSDs in the light precipitation mode (Pm : R > 0.5 mm h^{-1}) for the PARS and 2DVD at COR, SGP, and MAN sites. Tops and bottoms of boxes in blue solid line represent the 75th and 25th quartiles, respectively, and the horizontal red solid lines inside the boxes represent the median. PARS = second generation disdrometer, 2DVD = two-dimensional video disdrometer, COR = Córdoba; SGP = Southern Great Plains, and MAN = Manacapuru. 30
3.28 Box-and-whisker plots for the reflectivity factor (Z) in the light precipitation mode (Lpm : R < 0.5 mm h^{-1}) for the PARS and 2DVD at COR, SGP, and MAN sites. Tops and bottoms of boxes in blue solid line represent the 75th and 25th quartiles, respectively, and the horizontal red solid lines inside the boxes represent the median. PARS = second generation disdrometer, 2DVD = two-dimensional video disdrometer, COR = Córdoba; SGP = Southern Great Plains, and MAN = Manacapuru. 31
3.29 Box-and-whisker plots for the reflectivity factor (Z) in the light precipitation mode (Pm : R < 0.5 mm h^{-1}) for the PARS and 2DVD at COR, SGP, and MAN sites. Tops and bottoms of boxes in solid blue line represent the 75th and 25th quartiles, respectively, and the horizontal red solid lines inside the boxes represent the median. PARS = second generation disdrometer, 2DVD = two-dimensional video disdrometer, COR = Córdoba; SGP = Southern Great Plains, and MAN = Manacapuru. 31

List of Abbreviations

ARM	Atmospheric Radiation Measurement
AMF1	ARM Mobile Facility 1
BECAL	Becas Carlos Antonio López, Paraguay
CACTI	Cloud Aerosol, and Complex Terrain Interactions
COR	Córdoba, Argentina
DOE	Department of Energy
DSD	Drop size distribution
GoAmazon	Grean Ocean Amazon 2014/15
MAN	Manacapuru, Brazil
MAOS	Mobile Aerosol Observing System
NSF	National Science Foundation
RELAMPAGO	Remote sensing of Electrification, Lightning, And Mesoscale/microscale Processes with Adaptative Ground Observations 2018/19
SDC	Sierras de Córdoba, Argentina
SGP	Southern Great Plains, United States of America
TRMM	Tropical Rainfall Measuring Mission

Chapter 1

Introduction

More than 50 years of satellite observations have revealed that 67% of the earth's surface exhibits cloud cover, and those clouds play a dominant role in the global radiation balance. Clouds drive the atmospheric circulation from the global to convective scales through diabatic heat release. Besides the heating and cooling due to radiative effects, turbulence, and the phase changes of water, clouds also moderate the global hydrological cycle through precipitation processes and by transporting water vertically (Baker, 1997; Jakob and Miller, 2003; Paukert et al., 2019).

The microphysical processes that modify the cloud structure and lifetime, as well as control the redistribution of heat and moisture generated by cloud systems, are linked to the underlying thermodynamic conditions arising largely from vertical air motions within and outside the cloud system (Lloyd et al., 2014; Sui et al., 2007; Williams, 1995). Understanding the connections between the kinematic and thermodynamic conditions that influence the microphysical processes in clouds and attendant rainfall production is important from a hydrometeorological perspective, but these intertwined processes that operate from microphysical to mesoscales can be difficult to represent with fidelity in multi-scale atmospheric models (Emanuel, 1994; Jakob and Miller, 2003; Jakob, 2003; Paukert et al., 2019).

Liquid precipitation can be characterized by its drop size distribution (DSD) and DSD observations are of interest in applications beyond understanding the roles of microphysical processes in clouds. For example, for rainfall estimation satellite-based or ground-based retrieval algorithms, DSDs are critical for determining reflectivity-rain rate relations (Chandrasekar and Bringi, 1987; Atlas and Ulbrich, 1990; Joss et al., 1990; Uijlenhoet and Pomeroy, 2001; Rosenfeld and Ulbrich, 2003) or improving dual-polarization rainfall retrievals (Bringi and Chandrasekar, 2001; Krajewski and Smith, 2002; Berne and Krajewski, 2013; Rauber and Nesbitt, 2018). Additionally, the characterization of DSDs in multi-scale models is important in the representation of dynamic processes and rainfall prediction in model simulations and forecasts, impacting hydrometeorological predictions, as well as for studies of soil erosion by rainfall and irrigation systems in the agronomic sciences and in agricultural engineering (Rosewell, 1986; Caracciolo et al., 2012; Williams et al., 2014; Gong et al., 2014; Vaughan et al., 2015; Duan et al., 2019).

Various mathematical models have been formulated to quantify the raindrop size distribution shape characteristics, such as the exponential distribution $N(D) = N_0 \exp(-\lambda D)$, where $N(D)$ is the raindrop concentration per droplet diameter D (mm) interval per unit of volume (m^{-3} mm^{-1}); N_0 (m^{-3} mm^{-1}) is the intercept parameter; λ (mm^{-1}) is the slope parameter, as first formulated by Marshall and Palmer (Marshall and Palmer, 1948). Moreover, the three-parameter gamma distribution $N(D) = N_0 D^{\mu} \exp(-\lambda D)$, where N_0 (m^{-3} $mm^{-1-\mu}$); μ (unitless), and λ (mm^{-1}), as introduced by Ulbrich (Ulbrich, 1983) and Willis (Willis, 1984), but with a disadvantage that the three parameters are mathematical and not easily interpretable physical quantities.

To overcome this disadvantage, Testud et al. (Testud et al., 2001) proposed the normalization of raindrop distribution without *a priori* assumption about the DSD shape and finding a normalized intercept parameter N_0^* (or N_w) proportional to LWC and (D_m^{-4}), where LWC is the liquid precipitation water content (g m^{-3}) and D_m is the equivalent spherical diameter (mm). So, these three quantities in the normalized Gamma DSD are more physical quantities: N_w, D_m, and μ, representing the intercept parameter of an exponential distribution with same LWC and D_m, median mass diameter, and shape parameter of 0.

Radar hydrometeorology is dependent on the estimation of raindrop size distribution (DSD) as a function of rain physics parameters through the $Z = aR^b$ relationships, where Z is the radar reflectivity factor (typically expressed in dBZ units, where $dBZ = 10 \log_{10} Z$); R is the rain rate (mm h^{-1}), a and b are empirical quantities dependent on the DSD variability for different rain types and regimes due to differences in their dominant microphysical processes (Seliga and Bringi, 1976; Ulbrich and Atlas, 1978; Wilson and Brandes, 1979; Ulbrich, 1983; Bringi et al., 2003; Deo and Walsh, 2016).

Apart from Z, other radar parameters for which the DSD is relevant, are the differential reflectivity factor Z_{dr} associated with the reflectivity-weighted mean diameter (D_z), where D_z is defined as the ratio of the 7th and 6th moments of the DSD (Thurai and Bringi, 2008). The linear depolarization ratio L_{DR} is proportional to (D_z^2), while the co-polar correlation coefficient (ρ_{co}) related to D_z and D_z's variance, all three of these polarimetric quantities defined by (Bringi and Chandrasekar, 2001). Also, the specific differential phase K_{dp} is proportional to LWC and N_0, and is a polarimetric quantity less sensitive to D_m and variations in the large drop end of the DSD (Bringi and Chandrasekar, 2001). For more details of these radar parameters and others, see subsection 7.1.4 in (Bringi and Chandrasekar, 2001).

The diverse $Z - R$ relationships found in the literature also imply different values of N_w depending on the microphysical processes occurring in rainfall in varying climate regimes (Ulbrich, 1983; Testud et al., 2001; Bringi et al., 2003; Dolan et al., 2018). In an attempt to classify surface rainfall using the DSD into convective and stratiform rainfall modes (which are produced by different microphysical processes and

thermodynamic conditions), Bringi et al. (Bringi et al., 2003, 2009) analyzed the linear relation between N_w (or $log_{10}\ N_w$) and median raindrop diameter (D_0), revealing microphysical differences in the stratiform and convective rain attributed to its formation processes, and introduced a convective-stratiform segregation criterion based on these two parameters for ten maritime and continental geographical locations.

Thompson et al. (Thompson et al., 2015) examined DSD observations in stratiform tropical oceanic rain at two locations and showed similar DSD characteristics for stratiform tropical oceanic rain as Bringi et al., except finding a larger N_w ($log_{10}\ N_w = 4.0-4.1$) at smaller D_0 ($0.7-1.1$ mm) in convective rain, contradicting previous studies up to that point for continental locations where the convective clusters presented smaller N_w ($log_{10}\ N_w = 3.0-3.5$) at smaller D_0 ($2.0-2.75$ mm). Bringi et al. (2003, 2009), (Thurai et al., 2010; Penide et al., 2013; Dolan et al., 2018). Together, two convective-stratiform rainfall separator lines will be examined in this study: $log_{10}\ N_w = 1.6D_0 + 6.3$ and $log_{10}\ N_w = 3.85$, determined by Bringi et al. (Bringi et al., 2009) and Thompson et al.(Thompson et al., 2015), respectively, however in different climate regimes that may cause these classifications to vary in their ability to describe these to describe these important rainfall modes.

In a global approach, Dolan et al. (Dolan et al., 2018) used the statistical technique of principal component analysis to examine the spatial-temporal variability in DSD datasets in twelve geographical locations from high latitudes to the tropics and present a conceptual model of the variability between N_w and D_0 based on clustering dominant microphysical processes that modify the DSD shape for different modes of rainfall. All sites reported larger N_w ($log_{10}\ N_w = 3.8-4.0$) in the high latitudes and smaller N_w ($log_{10}\ N_w = 3.0-3.5$) in the mid-latitudes. The two sites examined therein in the tropics reported a bimodality of N_w (maximum $log_{10}\ N_w$ at 3.4 and 4.0) for convective and stratiform rain clusters, and larger N_w($log_{10}\ N_w = 4.0-4.5$) at smaller D_0 (1.5 mm).

Another global examination of DSD properties from Gatlin et al. (Gatlin et al., 2015) analyzed samples of large drops from eighteen geographical sites in a variety of rainfall conditions, reporting raindrop maximum diameter values (D_{max}) up to $9.0-9.7$ mm for validation of D_{max} assumptions in remote sensing retrieval algorithms. Furthermore, Thurai et al. (Thurai et al., 2017) examined the effects of small drops from a two-instrument combined raindrop size spectrum at two sites in the U.S., showing evidence of a lower D_m, higher width mass spectrum (σ_M), and higher ratio σ_M/D_m that is another shape parameter (Bringi and Chandrasekar, 2001; Thurai and Bringi, 2008). A drizzle and precipitation modes were also observed in the combined spectra, along with higher values of N_w due to raindrop minimum diameters values ($D_{min} < 0.7$ mm) that are generally undercounted by commonly-used disdrometers.

Despite all disdrometer-based efforts to measure surface precipitation and improve the precipitation rep-

resentation around the world, a search throughout the broad DSD literature indicates that there is still a lack of disdrometer measurements globally (Chase et al., 2020) and in particular, in South America. However, some important DSD observations have been collected in Brazil's Amazon Basin, from campaigns by the NASA Tropical Rainfall Measuring Mission-Large Scale Biosphere-Atmosphere (TRMM-LBA) experiment conducted in southwestern Amazonia (1999) Tokay et al. (2002, 2013), (Martins et al., 2010; Gatlin et al., 2015), and the Department of Energy (DOE) Atmospheric Radiation (ARM) Green Ocean Amazon (GoAmazon) field campaign conducted in central Amazonia (during the two wet seasons of 2014 and 2015) (Giangrande et al., 2016; Martin et al., 2016b; Wang et al., 2018). Moreover, the DOE ARM Clouds, Aerosols, and Complex Terrain Interactions (CACTI) and the Remote sensing of Electrification, Lightning, And Mesoscale/microscale Processes with Adaptive Ground Observations (RELAMPAGO) field campaigns (conducted during the warm season of 2018-9) collected novel disdrometer observations in west central Argentina, near the Sierras de Córdoba (a north-south oriented mountain range east of the Andes known to frequently initiate deep convection) (Nesbitt and coauthors, 2016; Mulholland et al., 2018, 2019; Varble et al., 2019b; Cancelada et al., 2020).

Precipitation processes in subtropical South America may be unique to those collected in other climate regimes: observations from the Precipitation Radar (PR) aboard the TRMM satellite have shown that the deep convective regions in subtropical South America produce among the most intense and organized convective systems on Earth (Zipser et al., 2006; Nesbitt et al., 2006). Previous studies have compared the vertical and horizontal radar reflectivity echo structures of three deep convection regions in the Americas including the Amazon and west central Argentina, by examining an 11-year record of storms from the TRMM PR dataset (Romatschke and Houze Jr, 2010; Rasmussen and Houze Jr, 2011; Rasmussen et al., 2014, 2016; Mulholland et al., 2018). For example, Rasmussen et al. (Rasmussen and Houze Jr, 2011) suggested that organized convective systems bearing wide convective cores are more frequent near the Sierras de Córdoba (SDC) in west central Argentina, where the RELAMPAGO-CACTI field campaign took place. Also, that this frequent organized convection presents similarities with the mesoscale convective system (MCS) structure of a leading line of cells followed by a stratiform rain region observed in Central Oklahoma in the United States (Rutledge et al., 1988), however storms in the Great Plains do not interact significantly with topography in contrast with storms near the SDC. In the Amazon, Romatschke and Houze Jr (2010) and Rasmussen and Houze Jr (2011), indicated that deep convective cores are relatively infrequent over the Amazon region compared with the warm season storms in subtropical South America and the Great Plains, thus, they have classified convective systems more commonly in a broad stratiform category during the Amazonian wet season.

The purpose of this thesis is to leverage these recent data collection efforts and examine the compilation of disdrometer datasets for comparisons of DSDs and the DSD parameters among three deep convective regions in the Americas: west central Argentina during the RELAMPAGO-CACTI field campaign, from the U.S. Southern Great Plains site, both in the American midlatitudes, and central Amazonia during the GoAmazon field campaign, in the American tropics. Therefore, it is intended to answer from these comparisons, the following specific questions:

1. How do DSD observations and the relationships between the DSD parameters compare among these 3 sites in the Americas?

2. What can the inferences of rain formation processes and vertical radar echoes contribute to enhance our analysis of the precipitation observed at Córdoba site in Argentina?

3. How do the raindrop distribution shape parameters within this data compilation compare with others observed in previous studies?

The results obtained from this comparison are summarized in two parts: Questions 1-2 in Sections 3.1-3.2 (also available in Rivelli Zea and Nesbitt 2020, in review), and Question 3 in Section 3.3. The results altogether are discussed in Section 4. The data and methods are outlined in Section 2, and the overall conclusions are presented in Section 5.

Chapter 2

Data and Methods

2.1 Location of sites

The three sites in the Americas here considered are spread across different climate regimes: humid subtropical grasslands for the U.S. Southern Great Plains, and complex terrain with humid subtropical climate for Córdoba, Argentina, to an equatorial rainforest in Manacapuru, Brazil. For these sites, the ground-based measurements compiled from the ARM user facility corresponds to the following field experiments (Fig. 2.1):

1. The Southern Great Plains (SGP) atmospheric observatory is the largest field with extensive instrumentation deployed in the U.S. by the ARM Program (operating since 1992); located in north-central Oklahoma, on the southwest part of the Mississippi Basin. This is the second largest basin in the Americas after the Amazon, where extreme flood events during the spring-summer seasons of 1993 (Karl and Knight, 1998; Wolf et al., 1999; Barraqué, 2017). Houze et al. (Houze Jr et al., 1990) studied spring storm events in central Oklahoma from a six-year dataset, primary classifying them as MCSs producing significant rainfall, and showing the classical MCS structure of a leading line of convective cells trailed by stratiform rain.

2. The DOE ARM Green Ocean Amazon (GoAmazon) field campaign took place in the environmental conditions of Manaus, Brazil, in the central part of the Amazon Basin during the wet season of 2014-2015. The Amazon is the largest and broadly studied basin in the Americas (Nobre, 1984; Gat and Matsui, 1991; Wolf et al., 1999; Valverde and Marengo, 2014), considered an important convective area in the tropics where moderately intense to weak convective systems are the cause of major rainfall throughout the austral summer (Nesbitt et al., 2000; Zipser et al., 2006; Nesbitt et al., 2006; Nunes et al., 2016a; Marengo et al., 2017; Braga et al., 2017). The ARM Mobile Facility (AMF1) and Mobile Aerosol Observing System (MAOS) were in a site near Manacapuru ("T3"), on the Amazon River, located 80 km west from Manaus airport (Martin et al., 2016a,b; Giangrande et al., 2016; Wang et al., 2018).

3. The DOE ARM CACTI field campaign in conjunction with the National Science Foundation (NSF)-led RELAMPAGO field campaign, collected disdrometer observations from a number of sites across central Argentina. Both experiments took place in the environmental conditions of Córdoba, Argentina, near the Sierras de Córdoba (SDC) during the wet season of 2018-2019. Watercourses that have origin in the SDC form the Carcarañá River Basin that contributes its riverine water to the Paraná River, which is a major river in the La Plata Basin, the third largest basin in the Americas (Wolf et al., 1999; Collins et al., 2011; Chug and Dominguez, 2019). These rivers are a vital for different socioeconomic activities in the region, but also highly influenced by frequent intense, organized convection and consequent severe weather impacts including costly flooding disasters (Rasmussen et al., 2014; Lozada et al., 2015; Stenta et al., 2016; Bazán et al., 2018; Pal et al., 2019). The ARM Mobile Facility-1 (AMF1) site was located in Villa Yacanto de Calamuchita, located about 20 km to the east of the highest terrain of the SDC, also 100 km southwest from the major city of Córdoba (Varble et al., 2019a,b; Hardin et al., 2020).

2.2 Disdrometer instrumentation

Since 2006, the ARM Program has been collecting disdrometer-based measurements of the rainfall and corresponding DSDs towards a better understanding of the processes resulting in precipitation (Bartholomew, 2014, 2017). For the observation periods and experiments selected here, that is, between 2014 and 2019, and, for the SGP, GoAmazon, and CACTI-RELAMPAGO field campaigns, the ARM Program deployed two types of disdrometers for long-term measurements of DSDs. These are a particle size velocity (Parsivel2) laser optical disdrometer, and a two-dimensional video disdrometer (Schumacher, 2016; Dolan et al., 2018; Varble et al., 2019b).

The Parsivel2 disdrometer, henceforth PARS, provides measurements of the particle size distribution and fall speed distribution, from which surface precipitation as rainfall rate (R), liquid water content (LWC), number concentration, and raindrop characteristic size such as median volume diameter (D_0), and fall speed distribution can be derived (Löffler-Mang and Joss, 2000; Tokay et al., 2013; Bartholomew, 2014). The PARS is known for its robustness and low maintenance requirement in the field (Bartholomew, 2014), but also may have a tendency to overestimate the concentration of smaller raindrops in light rain and larger raindrops in heavy rain (Dolan et al., 2018; Giangrande et al., 2019). Further information about the PARS and its deployment can be found in the ARM Parsivel2 Handbook (Bartholomew, 2014), the reports from GoAmazon and CACTI field campaigns (Schumacher, 2016; Varble et al., 2019b), and recent studies using

ARM data (Dolan et al., 2018; Giangrande et al., 2019).

The two-dimensional video disdrometer, hereafter 2DVD, measures raindrop size, raindrop shape and fall speed (Tokay et al., 2013; Gatlin et al., 2015; Bartholomew, 2017). The 2DVD requires frequent calibration and tends to underestimate small droplet concentration (Gatlin et al., 2015; Thurai et al., 2017; Dolan et al., 2018). However, it provides the most accurate concentration of large raindrops and characterization of raindrop shape (Thurai et al., 2011; Tokay et al., 2013; Gatlin et al., 2015; Thurai et al., 2017; Rauber and Nesbitt, 2018). More details on the 2DVD and its deployment can be found in the ARM VDIS Instrument Handbook (Bartholomew, 2017), the CACTI field campaign report (Varble et al., 2019b), and previous studies using ARM datasets (Thompson et al., 2015; Dolan et al., 2018; Giangrande et al., 2019).

Table 2.1 presents an overview of the disdrometer datasets compiled during the wet season, and details about each deployment. For the DSDs comparisons, all instruments have recorded 1-min DSDs and 0.2-mm-width diameter bins spacing was also considered. DSD parameters have been calculated, including liquid water content LWC (g m^{-3}), the normalized gamma function parameters as the normalized intercept parameter N_w (m^{-3} mm^{-1}), the mass-weighted mean diameter D_m (mm), and the mass standard deviation σ_m (mm) (Testud et al., 2001; Williams et al., 2014).

Following the corrections applied in similar DSD studies (Tokay et al., 2013, 2014; Gatlin et al., 2015; Giangrande et al., 2019), the dataset processing have considered for each 1-min raindrop spectra, no drop sizes D_0 smaller than 0.3 mm diameter (Tokay et al., 2013, 2014) and rain rates R no lower than 0.1 mm h^{-1} in at least 5-min of consecutive rain, following (Giangrande et al., 2019). Previous studies found the above data processing to be more accurate for moderate to larger raindrops due to the disdrometers resolution ($\sim$ 0.2 mm) and attendant tendency to underestimate the small raindrop concentration (Tokay et al., 2013; Giangrande et al., 2019; Thurai et al., 2017).

A second stage of the data quality control have included a subset of 1-min observations with at least 100 drops (Thompson et al., 2015; Dolan et al., 2018; Giangrande et al., 2019). Rain rates R lower than 0.5 mm h^{-1}, and median raindrop diameters D_0 no less than 0.3 and no greater than 4.75 mm were considered for what is defined as "light precipitation mode" (Lpm) following (Thurai et al., 2017). Rain rates R greater than 0.5 mm h^{-1}, and raindrops D_0 no smaller than 0.5 and no greater than 9.5 mm were the considerations for what is defined as "precipitation mode" (Pm) (Caracciolo et al., 2008; Gatlin et al., 2015; Thurai et al., 2017). Additionally, time-height scans of reflectivity (dBZ) from the Ka-band ARM Zenith Radar (KAZR) zenith-pointing Doppler cloud radar deployed for CACTI were used to investigate Lpm and Pm cases over the disdrometers' site at COR.

Furthermore, polarimetric radar parameters were computed using the T-matrix numerical method for

the 1-min DSDs from each site. Polarimetric quantities such as the reflectivity factor (Z, dBZ), differential reflectivity (Zdr, dB), linear depolarization ratio (L_{DR}, dB), the specific differential phase (Kdp, $deg\ km^{-1}$) and others, were calculated. The T-matrix simulations at C-band (5.5 GHz) set water temperature of 20° C (Bringi and Chandrasekar, 2001; Thurai and Bringi, 2008), maximum diameter at 9.5 mm, a droplet Gaussian canting angle with 0° mean and 7° standard deviation (Rauber and Nesbitt, 2018), and a drop size-shape model e.g. Thurai et al. (2007, 2009).

Alternatively, to analize the correlation of the reflectivity factor (Z, dBZ), rain rate ($log_{10}\ R$, dBR), and the width mass spectrum (σ_M, mm) as function of the mass spectrum mean diameter (D_m, mm) using the method described in (Williams et al., 2014), a third filtering was applied to our disdrometer observations compilation. First, this filtering classified each 1-min DSD in the light precipitation-precipitation mode ($Lpm - Pm$), corresponding to the part of the spectrum with at least 50 drops in 5-min of consecutive rain greater than 0.10 mm h^{-1}, median raindrop diameters D_0 no less than 0.30 and no greater than 4.75 mm, and reflectivity factor Z greater than 10 dBZ. Second, this alternative filtering classified the DSDs in the precipitation mode (Pm), for the part of the spectrum with at least 50 drops in 5-min of consecutive rain greater than 0.50 mm h^{-1}, median raindrop diameters D_0 no less than 0.50 and no greater than 9.50 mm, and reflectivity factor Z greater than 10 dBZ.

Table 2.1: Summary of the disdrometer datasets compiled for this study.

Site ID	Field campaign	City, State / Province, Country	Latitude, Longitude, Altitude (m)	Instrument	Rainy minutes	Data period selected
SGP	Southern Great Plains	Lamont, Oklahoma, United States	36.666 -97.624 311.50	PARS	22521	15 Apr – 30 Sep 2017 15 Apr – 30 Sep 2018 15 Apr – 11 Sep 2019
			36.605 -97.485 318.0	2DVD	21374	15 Apr – 30 Sep 2017 15 Apr – 30 Sep 2018 15 Apr – 11 Sep 2019
MAN	GoAmazon	Manacapuru, Amazonia, Brazil	-3.213 -60.698 50.0	PARS	21141	15 Oct 2014 – 30 Apr 2015 15 Oct – 01 Dec 2015
COR	CACTI-Relámpago	Villa Yacanto, Córdoba, Argentina	-32.126 -64.728 1141.0	PARS	24985	15 Oct 2018 – 30 Apr 2019
			-32.126 -64.728 1141.0	2DVD	18600	15 Oct 2018 – 30 Apr 2019

The data are free access and available in ARM website at https://www.arm.gov

Figure 2.1: Three sites in the largest basins of the Americas with ARM observation available at SGP represents the Southern Great Plains site in Central Oklahoma, U.S. (2017-2019); MAN is the site of the GoAmazon experiment in Manacapuru, Brazil (2014-2015), and COR depicts the site of the CACTI experiment in Villa Yacanto, Argentina (2018-2019). SGP is in a grassland region in the mid latitudes within the Mississippi Basin (red region); MAN is in a region of tropical rain forest or the in tropics within the Amazon Basin (green region), and COR is in a region of complex terrain near the Sierras de Córdoba (SDC) in the mid latitudes within the La Plata Basin (cyan region).

Chapter 3

Results

3.1 DSD parameter statistical comparisons

To examine the site-to-site variability of selected DSD parameters, we present the probability density functions (pdfs) of rain rate, mass-weighted mean diameter as D_m (mm), maximum diameter as (D_{max}), and normalized intercept parameter as $log_{10}\ N_w$ (N_w units m^{-3} mm^{-1}). In Figures 3.1-3.16, the disdrometer datasets (PARS/2DVD) are indicated by light blue/blue lines at COR, dark red/orange lines at SGP, and by green lines at MAN. The figures 3.9-3.12 show pdfs with histograms of D_{max} indicated by light blue at COR, dark red at SGP, and by green lines at MAN.

Figure 3.1 shows the pdf of rain rate at the 3 sites from the two disdrometers, where available (displayed as 10 $log_{10}\ R$ in dBR, with R in mm hr^{-1}). When all rain observations are considered together, the rain rate pdfs appear quite similar, particularly at the midlatitude sites (COR and SGP), while at MAN, it was measured lower (higher) frequency of observed values between 0-5 (10-15) dBR corresponding with the rain rate range of 1-3 (10-30) mm h^{-1}. Despite general agreement, slight differences exist between COR and SGP in that COR site has slightly higher (lower) rain rate frequencies at 1(30) mm h^{-1}

Figures 3.2-3.4 examine 10 $log_{10}\ R$ rain rate pdfs at each site, separated by rainfall modes as described in section 2.

Overall, when separated between modes, the rain rate pdfs at each site appear to show distributions in the light precipitation mode (Lpm) right-skewed with a heavy right tail near the maximum rain rate cutoff, indicating a higher observed frequency of heavier rain in this mode, while distributions in the precipitation mode (Pm) left-skewed towards the minimum rain rate cutoff, indicating more frequent light rainfall in this mode.

At COR and SGP, the pdfs of R are quite similar between the PARS and 2DVD in both the Lpm and Pm. Also, the Lpm and Pm R distributions at SGP (Fig. 3.3) are remarkably similar to the Lpm and Pm R distributions at COR (Fig. 3.2). At MAN (Fig. 3.4), observations of R in the Lpm reveal higher rain rate frequencies, and in the Pm, a heavier tail of larger values of R than at SGP and COR, with an inflection

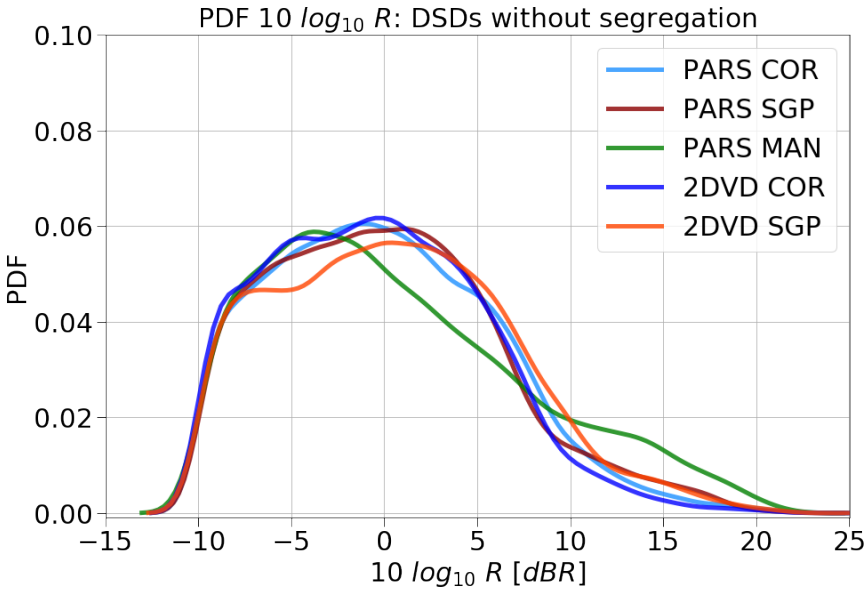

Figure 3.1: Rain rate (R) as 10 log_{10} R pdfs for DSDs without classification at COR (PARS/2DVD in light blue/blue lines); SGP (PARS/2DVD in dark red/orange lines), and MAN (PARS in green lines). DSDs = raindrop size distributions; PARS = second generation parsivel disdrometer, 2DVD = two-dimensional video disdrometer; COR = Córdoba; SGP = Southern Great Plains, and MAN = Manacapuru.

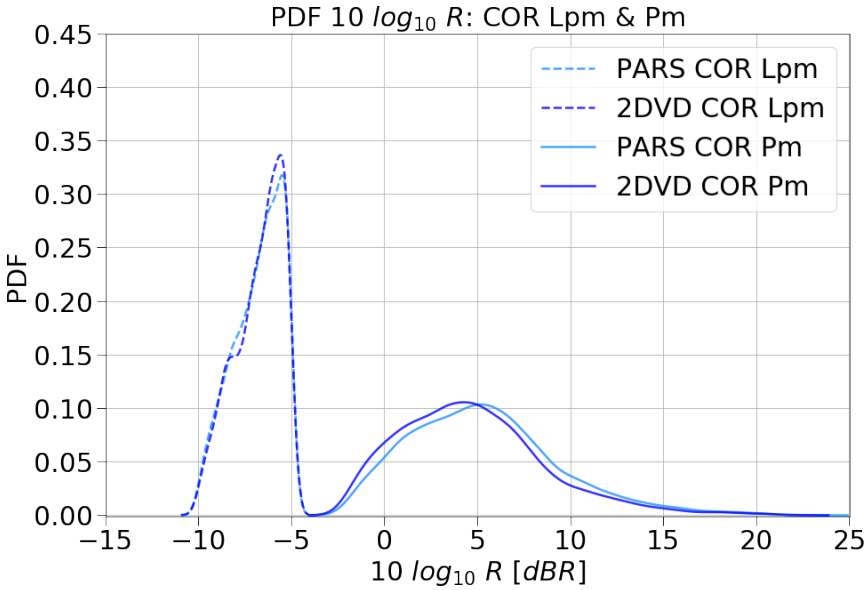

Figure 3.2: Rain rate (R) as 10 log_{10} R pdfs for DSDs classified into the light precipitation mode (Lpm : R < 0.5 mm h^{-1}) in dashed lines, and precipitation mode (Pm : R > 0.5 mm h^{-1}) in solid lines; at COR (PARS/2DVD in light blue/blue lines). DSDs = raindrop size distributions; PARS = second generation parsivel disdrometer, 2DVD = two-dimensional video disdrometer, and COR = Córdoba.

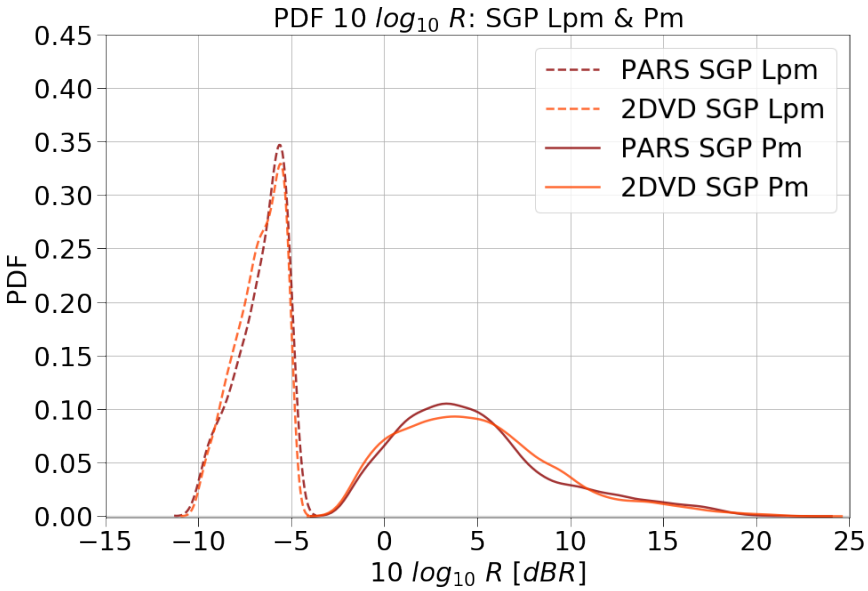

Figure 3.3: Rain rate (R) as 10 log_{10} R pdfs for DSDs classified into the light precipitation mode (Lpm : R < 0.5 mm h^{-1}) in dashed lines, and precipitation mode (Pm : R > 0.5 mm h^{-1}) in solid lines; at SGP (PARS/2DVD in dark red/orange lines). DSDs = raindrop size distributions; PARS = second generation parsivel disdrometer, 2DVD = two-dimensional video disdrometer, and SGP = Southern Great Plains.

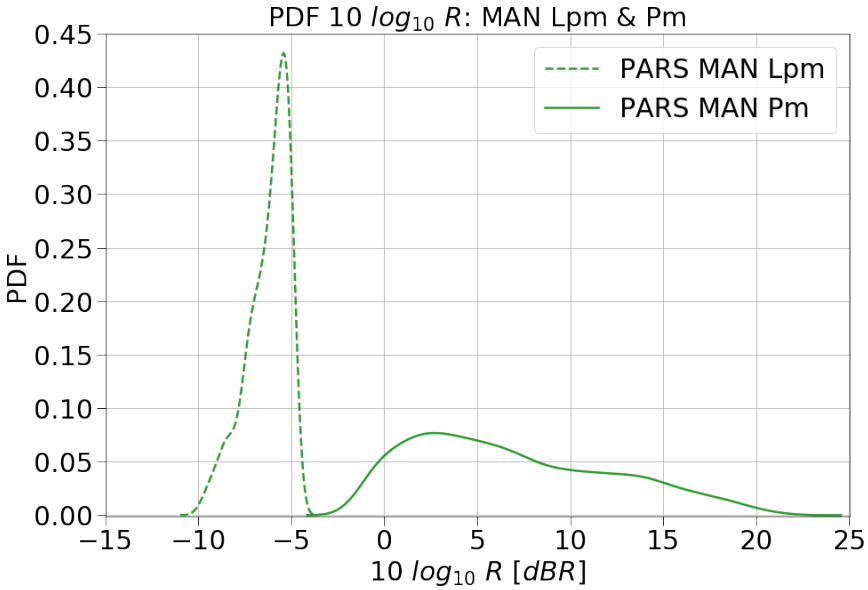

Figure 3.4: Rain rate (R) as 10 log_{10} R pdfs for DSDs classified into the light precipitation mode (Lpm : R < 0.5 mm h^{-1}) in dashed lines, and precipitation mode (Pm : R > 0.5 mm h^{-1}) in solid lines; at SGP (PARS/2DVD in dark red/orange lines). DSDs = raindrop size distributions; PARS = second generation parsivel disdrometer, 2DVD = two-dimensional video disdrometer, and and MAN = Manacapuru.

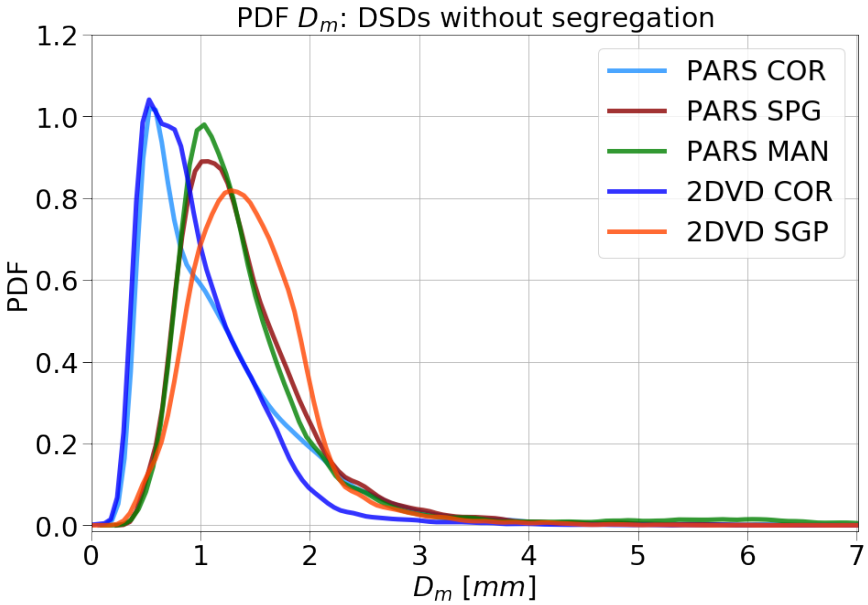

Figure 3.5: Mass-weighted mean diameter (D_m) pdfs for DSDs without classification at COR (PARS/2DVD in light blue/blue lines); SGP (PARS/2DVD in dark red/orange lines), and MAN (PARS in green lines). DSDs = raindrop size distributions; PARS = second generation parsivel disdrometer, 2DVD = two-dimensional video disdrometer; COR = Córdoba; SGP = Southern Great Plains, and MAN = Manacapuru.

point in the R distribution near 10 dBR (10 mm h^{-1}) and higher relative frequencies of R at 15 dBR (30 mm h^{-1})than the other two sites.

Figure 3.5 shows that pdfs of D_m at the 3 sites are similar, however, the COR D_m distributions are slightly left-skewed towards sizes of raindrop less than 1 mm, different from SGP and MAN that evidence higher D_m frequencies around 1 mm. Separating the D_m statistics into Lpm and Pm, Figures 3.6-3.8 reveal similar shapes of the Pm distributions of D_m across the three sites, with the 2DVD and PARS distributions having very similar shapes at COR and SGP. The PARS distributions in the Pm are nearly identical amongst the three sites. In the Lpm, more significant differences are apparent among the sites. Both the PARS and 2DVD at COR peak at the D_m bin centered at 0.50 mm, although the distribution magnitude are different in this bin, while at SGP and MAN PARS distributions peak in the Lpm at the bin located near 0.85 mm (with the SGP 2DVD distribution mode located at even higher values near 1 mm, with much of the distribution occurring at higher values of D_m than the COR Lpm D_m distribution).

The COR site also presented a higher density of raindrops with D_{max} between 0.3 and 1.0 mm for both PARS and 2DVD in the light precipitation mode, compared to MAN and SGP (Figs.3.9 and 3.10). These observations do not include light precipitation that may be missed by the PARS/2DVD (Thurai et al., 2017). Nevertheless, the presence of large drops was not accurately depicted due to some instrument discrepancies evidenced in the tail of the DSDs at this site (Figs.3.11 and 3.12).

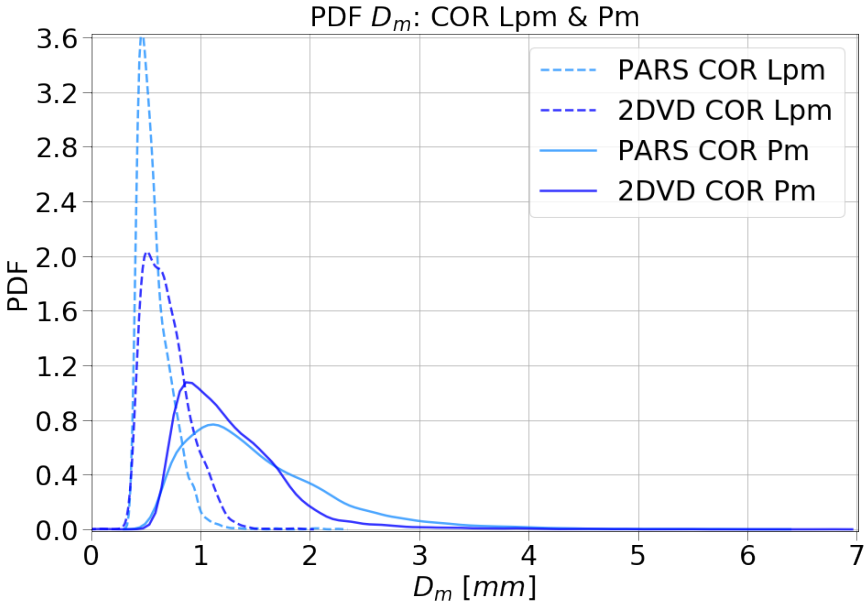

Figure 3.6: Mass-weighted mean diameter (D_m) pdfs for DSDs classified into the light precipitation mode (Lpm : R $<$ 0.5 mm h^{-1}) in dashed lines, and precipitation mode (Pm : R $>$ 0.5 mm h^{-1}) in solid lines; at COR (PARS/2DVD in light blue/blue lines). DSDs = raindrop size distributions; PARS = second generation parsivel disdrometer, 2DVD = two-dimensional video disdrometer, and COR = Córdoba.

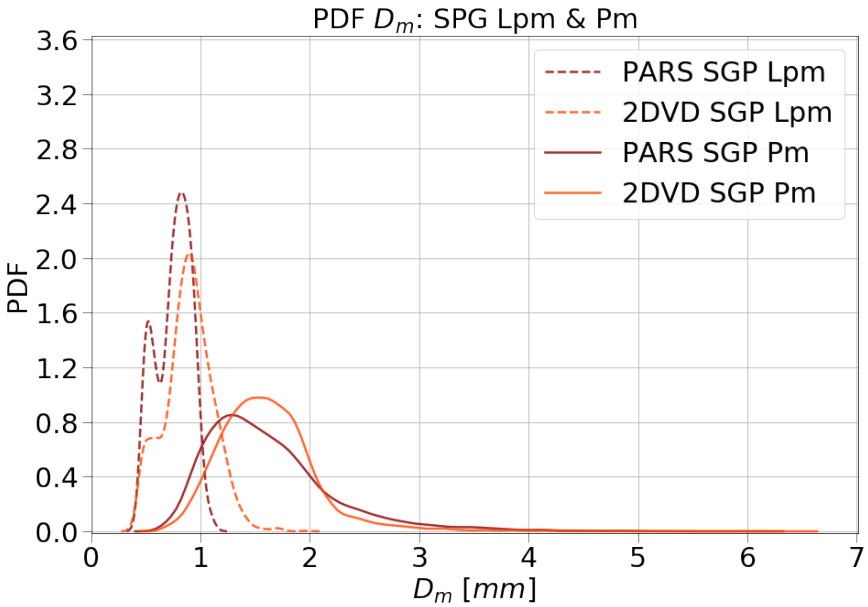

Figure 3.7: Mass-weighted mean diameter (D_m) pdfs for DSDs classified into the light precipitation mode (Lpm : R $<$ 0.5 mm h^{-1}) in dashed lines, and precipitation mode (Pm : R $>$ 0.5 mm h^{-1}) in solid lines; at SGP (PARS/2DVD in dark red/orange lines). DSDs = raindrop size distributions; PARS = second generation parsivel disdrometer, 2DVD = two-dimensional video disdrometer, and SGP = Southern Great Plains.

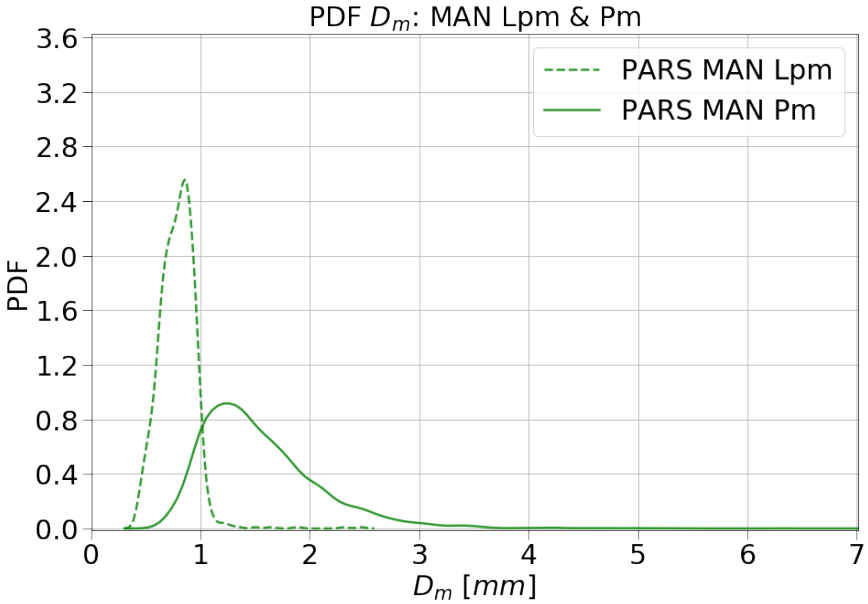

Figure 3.8: Rain rate (R) as 10 log_{10} R pdfs for DSDs classified into the light precipitation mode (Lpm : R < 0.5 mm h^{-1}) in dashed lines, and precipitation mode (Pm : R > 0.5 mm h^{-1}) in solid lines; at SGP (PARS/2DVD in dark red/orange lines). DSDs = raindrop size distributions; PARS = second generation parsivel disdrometer, 2DVD = two-dimensional video disdrometer, and and MAN = Manacapuru.

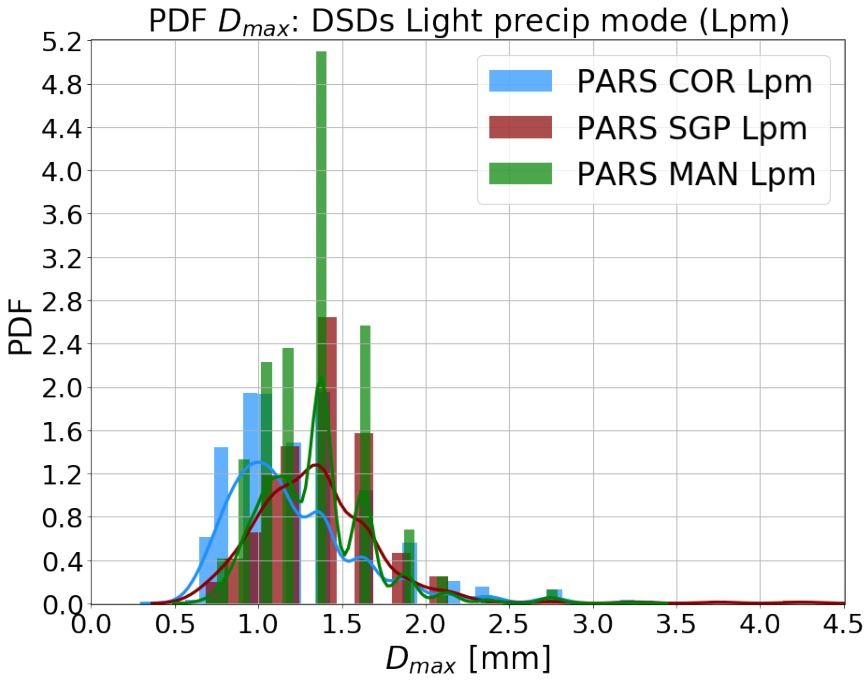

Figure 3.9: Density curves with histograms of the maximum diameter (D_{max}): DSDs in the light precipitation mode (Lpm : R < 0.5 mm h^{-1}) for the PARS at (a) COR, SGP, and MAN sites. DSDs = raindrop size distributions; PARS = second generation disdrometer; COR = Córdoba; SGP = Southern Great Plains, and MAN = Manacapuru.

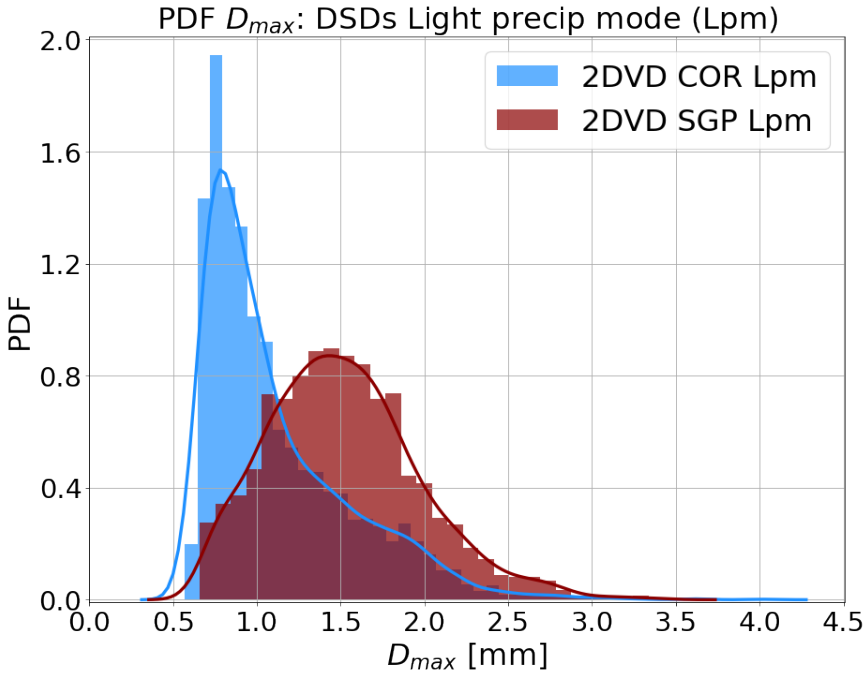

Figure 3.10: Density curves with histograms of the maximum diameter (D_{max}): DSDs in the light precipitation mode (Lpm : R < 0.5 mm h^{-1}) for the 2DVD at (a) COR, SGP, and MAN sites. DSDs = raindrop size distributions; 2DVD = two-dimensional video disdrometer; COR = Córdoba; SGP = Southern Great Plains, and MAN = Manacapuru.

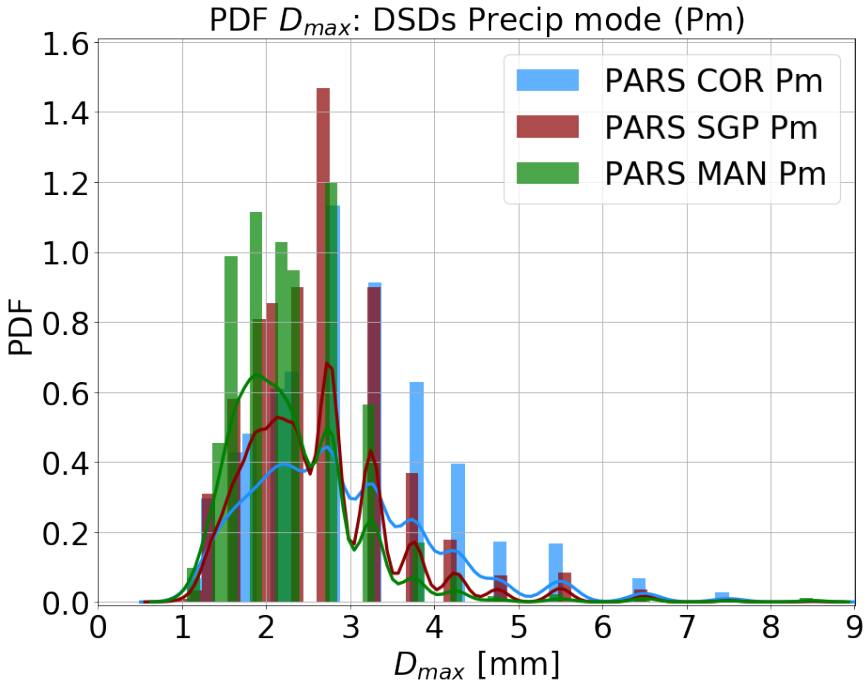

Figure 3.11: Density curves with histograms of the maximum diameter (D_{max}): DSDs in the precipitation mode (Pm : R > 0.5 mm h^{-1}) for the PARS at (a) COR, SGP, and MAN sites. DSDs = raindrop size distributions; PARS = second generation disdrometer; COR = Córdoba; SGP = Southern Great Plains, and MAN = Manacapuru.

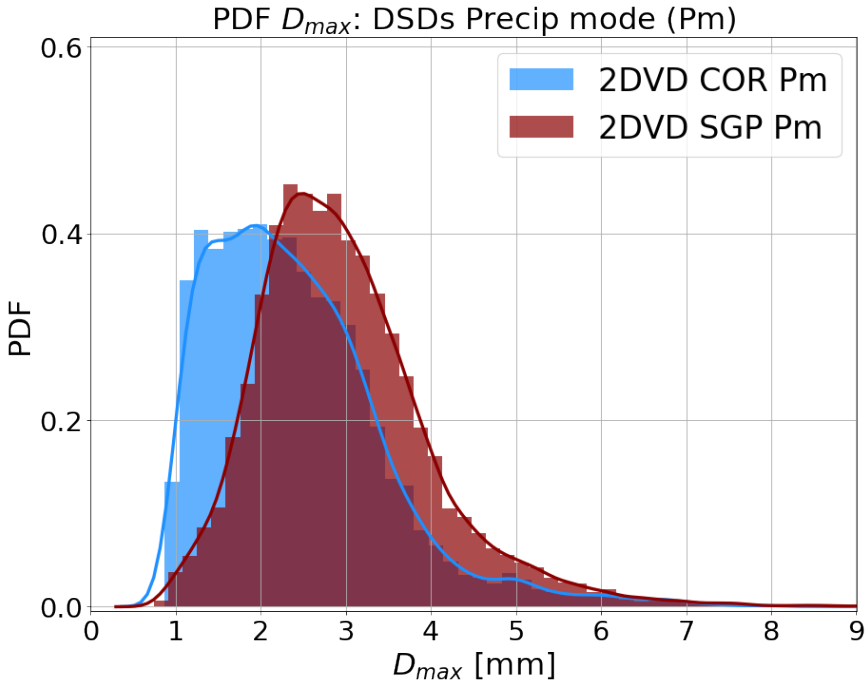

Figure 3.12: Density curves with histograms of the maximum diameter (D_{max}): DSDs in the precipitation mode (Pm : R $>$ 0.5 mm h^{-1}) for the PARS at (a) COR, SGP, and MAN sites. DSDs = raindrop size distributions; 2DVD = two-dimensional video disdrometer; COR = Córdoba; SGP = Southern Great Plains, and MAN = Manacapuru.

To investigate the variability of normalized droplet concentration $log_{10}N_w$, Figure **??** displays pdfs of this quantity using the same color convention as above. Here, large differences are present in the pdfs of N_w among all the sites (Fig. 3.13), and in terms of the the modes of N_w (Figs. 3.14-3.16), as well as the breadth of the N_w distributions. At SGP (Fig. 3.15), both the PARS and 2DVD observations show a relatively confined distribution of N_w centered near $log_{10}N_w = 3.2$. At MAN (Fig. 3.16), the distribution is slightly more broad, with a mode of N_w that is slightly more peaked than at SGP (near $log_{10}N_w = 3.60$). Distinct behavior in N_w from the two other sites is observed at COR (Fig. 3.14), with a much broader distribution of N_w seen in both the PARS and 2DVD observations. The 2DVD observations in the Pm have a higher frequency of large values of N_w ($\sim log_{10}N_w = 4.4$) than the PARS ($\sim 3.70\ log_{10}N_w$), while in the Lpm, the PARS observed larger frequencies of $log_{10}N_w$ near 4.6 compared with the 2DVD, which observed a broader distribution of N_w.

3.2 DSDs comparisons in terms of joint 2D-histograms

To analyze the site-to-site co-variability of PSD parameters, Figures 3.17-3.20 present joint two-dimensional histograms of the normalized number of concentration as $log_{10}\ N_w$ versus mean raindrop diameter as D_0

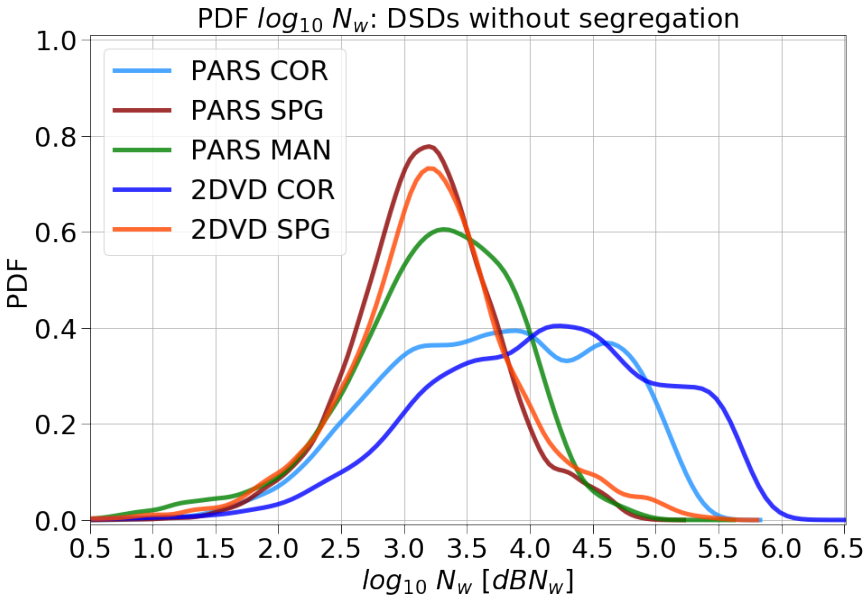

Figure 3.13: Normalized droplet concentration (N_w) as log_{10} N_w pdfs for DSDs without classification at COR (PARS/2DVD in light blue/blue lines); SGP (PARS/2DVD in dark red/orange lines), and MAN (PARS in green lines). DSDs = raindrop size distributions; PARS = second generation parsivel disdrometer, 2DVD = two-dimensional video disdrometer; COR = Córdoba; SGP = Southern Great Plains, and MAN = Manacapuru.

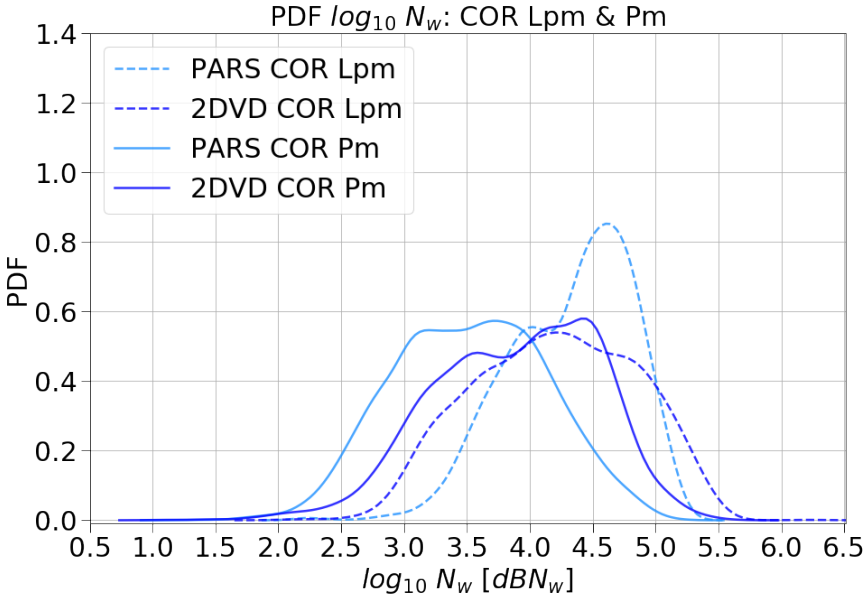

Figure 3.14: Normalized droplet concentration (N_w) as log_{10} N_w pdfs for DSDs classified into the light precipitation mode (Lpm : R ¡ 0.5 mm h^{-1}) in dashed lines, and precipitation mode (Pm : R > 0.5 mm h^{-1}) in solid lines; at COR (PARS/2DVD in light blue/blue lines). DSDs = raindrop size distributions; PARS = second generation parsivel disdrometer, 2DVD = two-dimensional video disdrometer, and COR = Córdoba.

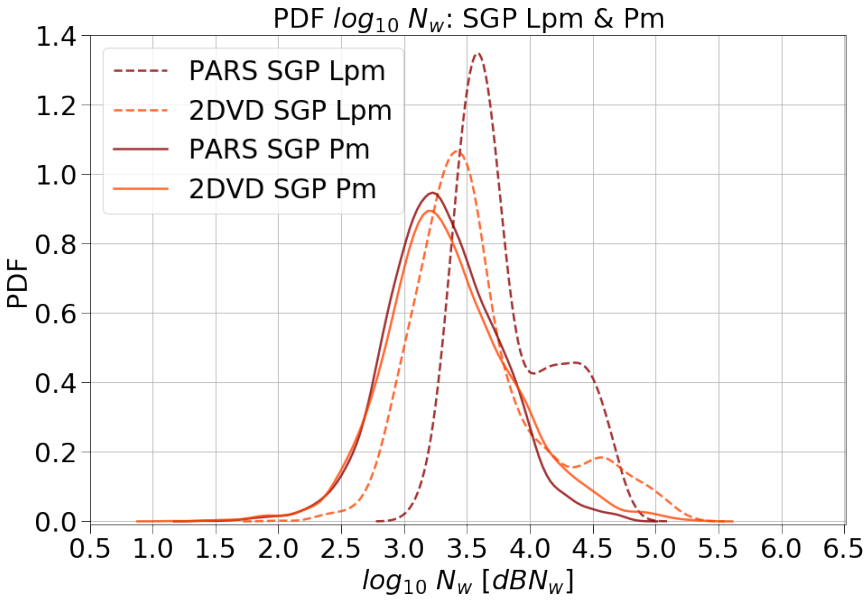

Figure 3.15: Normalized droplet concentration (N_w) as log_{10} N_w pdfs for DSDs classified into the light precipitation mode (Lpm : R $<$ 0.5 mm h^{-1}) in dashed lines, and precipitation mode (Pm : R $>$ 0.5 mm h^{-1}) in solid lines; at SGP (PARS/2DVD in dark red/orange lines). DSDs = raindrop size distributions; PARS = second generation parsivel disdrometer, 2DVD = two-dimensional video disdrometer, and SGP = Southern Great Plains.

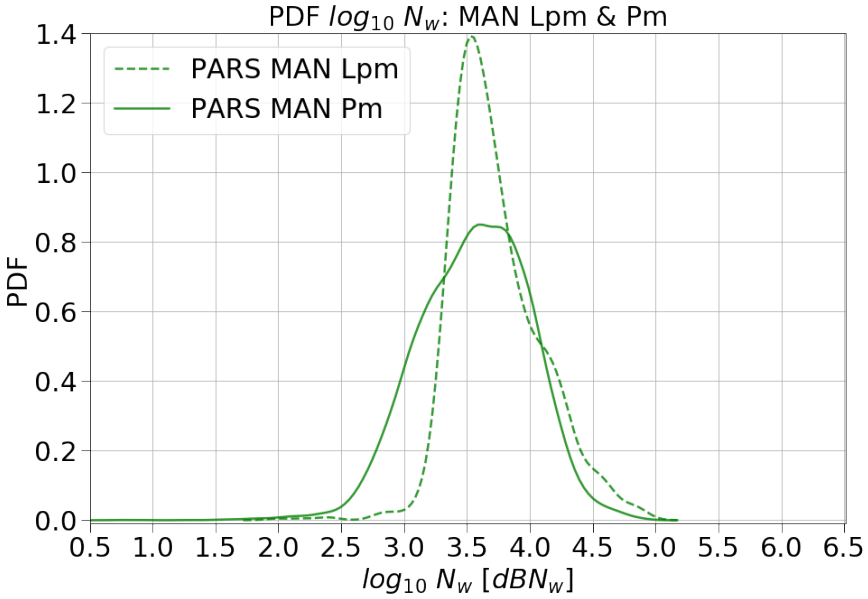

Figure 3.16: Normalized droplet concentration (N_w) as log_{10} N_w pdfs classified into the light precipitation mode (Lpm : R $<$ 0.5 mm h^{-1}) in dashed lines, and precipitation mode (Pm : R $>$ 0.5 mm h^{-1}) in solid lines; at SGP (PARS/2DVD in dark red/orange lines). DSDs = raindrop size distributions; PARS = second generation parsivel disdrometer, 2DVD = two-dimensional video disdrometer, and and MAN = Manacapuru.

(mm), and the two-dimensional histograms of the liquid water content (presented as $log_{10}\ LWC$ in g m^{-3}) versus median raindrop diameter as $log_{10}\ D_0$ (with D_0 in mm), separated by rainfall mode. The PARS data is indicated by color contours and the 2DVD data is indicated by color-dashed contours.

In Figure 3.18, the DSD parameter interrelationships are shown for each site in the precipitation mode (Pm). Each of the sites show a general inverse relationship between $log_{10}\ N_w$ and D_0 as shown by previous studies, as would be expected given the location of the sites being located in regions containing deep convective precipitation. The regions of highest observed probability of N_w and D_0 are close to each other at SGP and MAN (near a D_0 of 1.1 mm and $log_{10}\ N_w$ near 3.5, but higher at COR (near 0.9 mm and $log_{10}\ N_w$ 4.1 for D_0 and N_w, respectively). Beyond the overall shape of the distributions, there are key differences among these sites in the N_w–D_0 parameter space. Consistent with the results presented above, in the Pm, values of D_0 occupy ranges that are consistent amongst the sites in the Pm, but vary more in N_w. Two primary differences among the sites stand out in the Pm. The first is the large variability of N_w at COR compared with the other sites, which extends the distribution of observations in the N_w-D_0 space. In particular, the frequency of N_w observations above 10^5 mm^{-1} m^{-3} in both the PARS and 2DVD distribution at COR is unique relative to the other sites.

In terms of the relationship between LWC and D_0 in the Pm (Figure 3.20), the COR and SGP sites have very similar distributions, which holds true in both instruments (PARS and 2DVD). At MAN, the distribution of observations extends to both higher values of D_0 and LWC, which has been noted in tropical sites (Tokay and Short, 1996; Yuter and Houze Jr, 1997; Thompson et al., 2015; Dolan et al., 2018), however it is not as clearly defined as in the multi-site DSD composites shown in Dolan et al.(Dolan et al., 2018), possibly indicating the at-times continental nature of the convection observed in the Amazon Basin (Nunes et al., 2016b), despite its moniker as the "Green Ocean" yielding a reputation of having maritime-like convective intensity characteristics (Williams et al., 2002).

To further depict what types of precipitating systems are contributing to the relatively high observed droplet number concentrations at COR, cases of high N_w were manually examined and two representative cases are presented here. Figures 3.21 and 3.22 provide ARM Ka-band vertically-pointing radar scans collected over the COR site to show the vertical structure of radar echoes as well as the corresponding DSD parameters shown by the PARS disdrometer. Figure 3.21 shows a case of the light rain mode, where shallow precipitating clouds exist mostly below 1000 m above the site. These clouds, likely containing drizzle, do not precipitate at a detectable level of the PARS disdrometer until more than 4 hours after 1800 UTC (1500 local Argentine time), and during the time when precipitation is detectable, some weak convective generating cells appear present in these warm clouds (also in Doppler velocity, not shown). Values of log_{10}

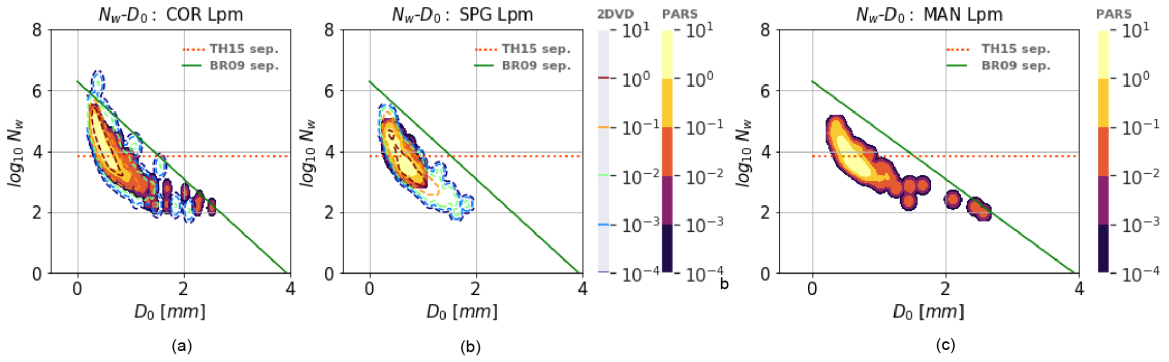

Figure 3.17: Two-dimensional frequency histograms for the normalized droplet concentration ($log_{10}\ N_w$) and mean raindrop diameter (D_0) in the light precipitation mode (Lpm) R ¡ 0.5 mm h^{-1} at (a) COR, (b) SGP, and (c) MAN sites. DSDs indicated by color contours for the PARS and color-dashed contours for the 2DVD. Lines from $BR09$ (solid green) and $TH15$ (dashed red) for convective-stratiform segregation.

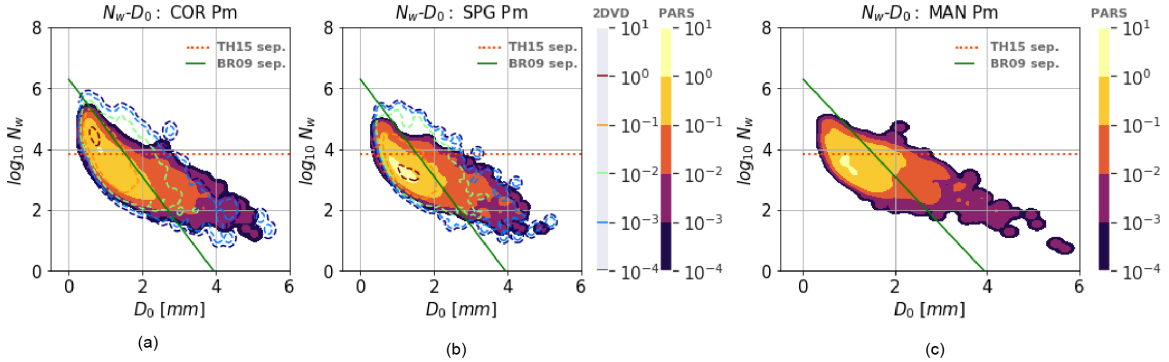

Figure 3.18: Two-dimensional frequency histograms for the normalized droplet concentration ($log_{10}\ N_w$) versus mean raindrop diameter (D_0) in the precipitation mode (Pm) R $>$ 0.5 mm h^{-1} at (a) COR, (b) SGP, and (c) MAN sites. DSDs indicated by color contours for the PARS and color-dashed contours for the 2DVD. Lines from $BR09$ (solid green) and $TH15$ (dashed red) for convective-stratiform segregation.

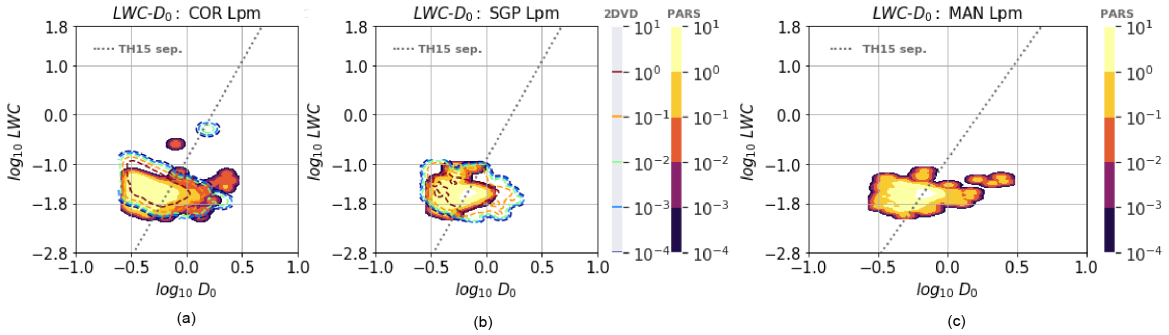

Figure 3.19: Two-dimensional frequency histograms for the liquid water content (LWC) as $log_{10}\ LWC$ versus mean raindrop diameter as $log_{10}\ D_0$ in the light precipitation mode (Lpm) R $<$ 0.5 mm h^{-1} at (a) COR, (b) SGP, and (c) MAN sites. DSDs indicated by color contours for the PARS and color-dashed contours for the 2DVD. Lines from $TH15$ (dashed gray) for convective-stratiform segregation.

N_w in m^{-3} mm^{-1} exceed 5 throughout much of the event, and though R varies from the Lpm into the Pm shortly before and after 0000 UTC (2100 local time). In another case that contained Lpm-classified time periods, Figure 3.22 presents a case where shallow Lpm exists between two deep convective core events. The first convective event occurred overnight near 0500 UTC or 0100 local time, with anvil clouds existing above 6 km for several hours above ground level above rain rates < 2 mm hr^{-1}, including some periods of Lpm near-surface precipitation). The next day, another afternoon convective event occurred near 1900 UTC or 1700 local time. Between these events, clouds, drizzle, and light precipitation with high log_{10} N_w and low D_0 occurred for more than 12 hours, and these clouds appear less obviously convective in reflectivity and Doppler velocity observations than the 28 Nov 2018 case. These unique DSD structures presented alongside their radar-determined vertical structure help to support the uniqueness of the COR observations especially in terms of the shallow vertical structures and high N_w values seen in both the Pm and Lpm rainfall modes in such cases. Future work will examine such cases in more detail.

3.3 Comparisons in terms of the DSD shape parameters

Without *a priori* assumption about the DSD shape, we analyze the site-to-site correlation of three DSD shape parameters described in (Williams et al., 2014). Figures 3.23-3.25 present the density of occurrence of these parameters. The reflectivity factor (Z, dBZ), rain rate (log_{10} R, dBR), and the width mass spectrum (σ_M, mm) as function of the mass spectrum mean diameter (D_m, mm) are DSD shape attributes considered in the $Lpm - Pm$ and Pm modes (i.e. for each 1-min DSD with at least 50 drops, $Lpm - Pm$: R > 0.10 mm h^{-1}) and $0.3 < D_0 < 4.75$ mm, and Pm : for R > 0.50 mm h^{-1} and $0.5 < D_0 < 9.50$ mm). Correlations are shown in tables 3.1-3.3 for discrepancies based on both Williams et. al (Williams et al., 2014) and the PARS/2DVD observations at the 3 sites. Greater divergence was found in rain rate at each location in both modes. More similar power law relations were obtained in σ_M at each location in $Lpm - Pm$ and Pm.

Moreover, for each 1-min DSD with at least 100 drops in the Lpm and Pm (i.e., Lpm : R < 0.5 mm h^{-1} and $0.3 < D_0 < 4.75$ mm, and Pm : R > 0.5 mm h^{-1} and $0.5 < D_0 < 9.50$ mm), and used to examine the relationship between D_{max} and D_m (Figs. 3.26-3.27). The D_m was calculated as the ratio of the fourth and third moments of the DSD. The raindrop maximum diameter (D_{max}) values were extracted from the disdrometer observations. Variations in the median values of the D_{max}/D_m ratio were found between 1.50 and 1.64 in the Lpm and, 1.7 and 1.9 in the Pm similar to 1.8 reported by Gatlin et al. (Gatlin et al., 2015).

Through figures 3.28-3.29 is possible to examine the reflectivity factor Z (i.e., sixth moment of the DSD in dBZ) for these 1-min DSDs with at least 100 drops in the Lpm and Pm (i.e., Lpm : R < 0.5 mm h^{-1}, 0.3

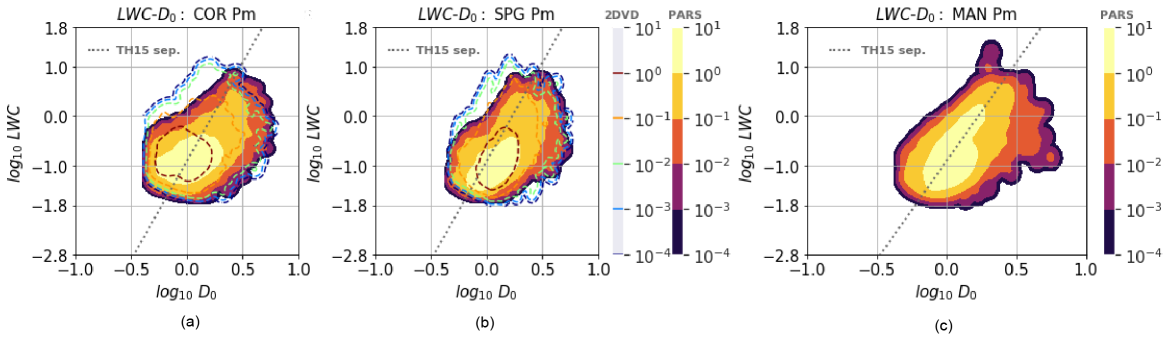

Figure 3.20: Two-dimensional frequency histograms for the liquid water content (LWC) as log_{10} LWC versus mean raindrop diameter as log_{10} D_0 in the precipitation mode (Pm) R $>$ 0.5 mm h^{-1} at (a) COR, (b) SGP, and (c) MAN sites. DSDs indicated by color contours for the PARS and color-dashed contours for the 2DVD. Lines from $TH15$ (dashed gray) for convective-stratiform segregation.

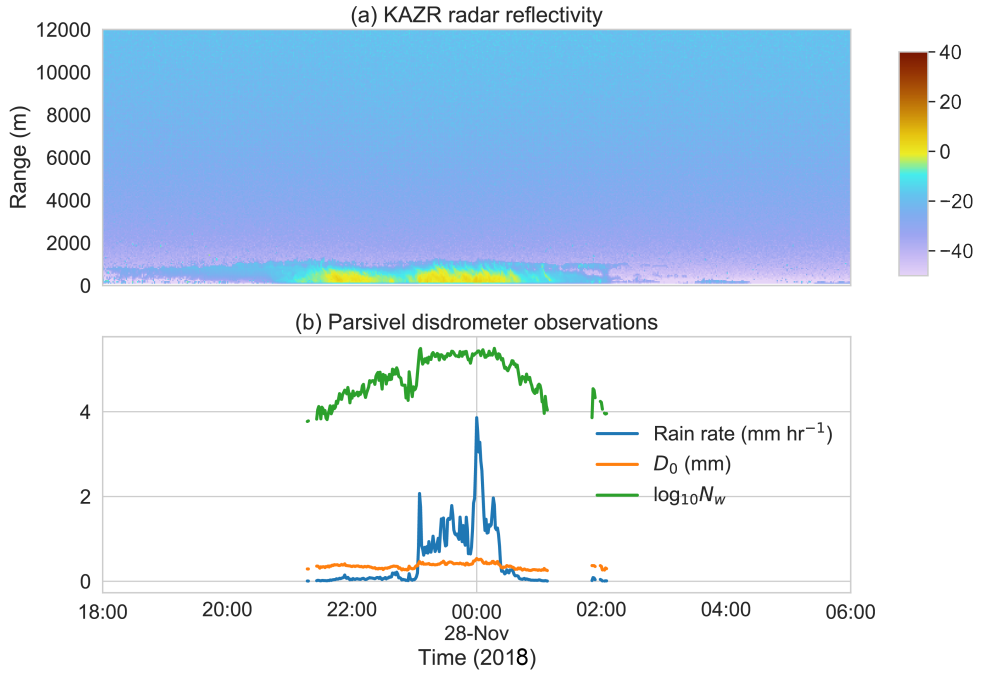

Figure 3.21: (a) ARM KAZR cloud radar radar reflectivity time-height scans over the COR site during CACTI, collocated with (b) DSD parameter calculations using PARS disdrometer data from 1800 UTC 27 Nov to 0600 UTC 28 Nov 2018.

$< D_0 < 4.75$ mm, and $Pm : \mathrm{R} > 0.5$ mm h^{-1}, $0.5 < D_0 < 9.50$ mm). The median of Z was found between 14 and 16.5 in the Lpm and, 26 and 32 dBZ in the Pm, different from the geometric median of 20.8 dBZ reported by Gatlin et al. (Gatlin et al., 2015).

Table 3.1: Overview of the correlation between the radar reflectivity factor Z and the mean mass diameter D_m observed in $Lpm - Pm$ and Pm. Power-law curves give by equations from $WL14$ = Williams et al. (Williams et al., 2014); PARS = parsivel disdrometer data, and the 2DVD = two-dimensional video disdrometer data.

Site Mode	Correlation from:	Z vs. D_m power law curve equation
	WL4	57.10 $log_{10}\ D_m$ + 22.88
$COR\ Lpm - Pm$	PARS	41.28 $log_{10}\ D_m$ + 25.03
	2DVD	34.85 $log_{10}\ D_m$ + 25.83
$SGP\ Lpm - Pm$	PARS	53.19 $log_{10}\ D_m$ + 21.85
	2DVD	50.77 $log_{10}\ D_m$ + 22.07
$MAN\ Lpm - Pm$	PARS	59.37 $log_{10}\ D_m$ + 22.53
$COR\ Pm$	PARS	43.54 $log_{10}\ D_m$ + 25.41
	2DVD	39.22 $log_{10}\ D_m$ + 26.77
$SGP\ Pm$	PARS	52.36 $log_{10}\ D_m$ + 22.61
	2DVD	48.09 $log_{10}\ D_m$ + 23.66
$MAN\ Pm$	PARS	5.75 $log_{10}\ D_m$ + 23.54

Table 3.2: Overview of the correlation between the rain rate (R) as 10 $log_{10}\ R$ and the mean mass diameter as D_m, observed in $Lpm - Pm$ and Pm. Power-law curves give by equations from $WL14$ = Williams et al. (2014); PARS = parsivel disdrometer data, and the 2DVD = two-dimensional video disdrometer data.

Site Mode	Correlation from:	R vs. D_m power law curve equation
	WL4	10 $log_{10}\ D_m^{3.14}$ + 0.061
$COR\ Lpm - Pm$	PARS	10 $log_{10}\ D_m^{1.59}$
	2DVD	34.85 $log_{10}\ {D_m}^{1.07}$
$SGP\ Lpm - Pm$	PARS	10 $log_{10}\ {D_m}^{2.13}$
	2DVD	10 $log_{10}\ {D_m}^{1.92}$
$MAN\ Lpm - Pm$	PARS	10 $log_{10}\ {D_m}^{3.12}$
$COR\ Pm$	PARS	10 $log_{10}\ {D_m}^{2.12}$
	2DVD	10 $log_{10}\ {D_m}^{1.93}$
$SGP\ Pm$	PARS	10 $log_{10}\ {D_m}^{2.20}$
	2DVD	10 $log_{10}\ {D_m}^{2.14}$
$MAN\ Pm$	PARS	10 $log_{10}\ {D_m}^{3.16}$

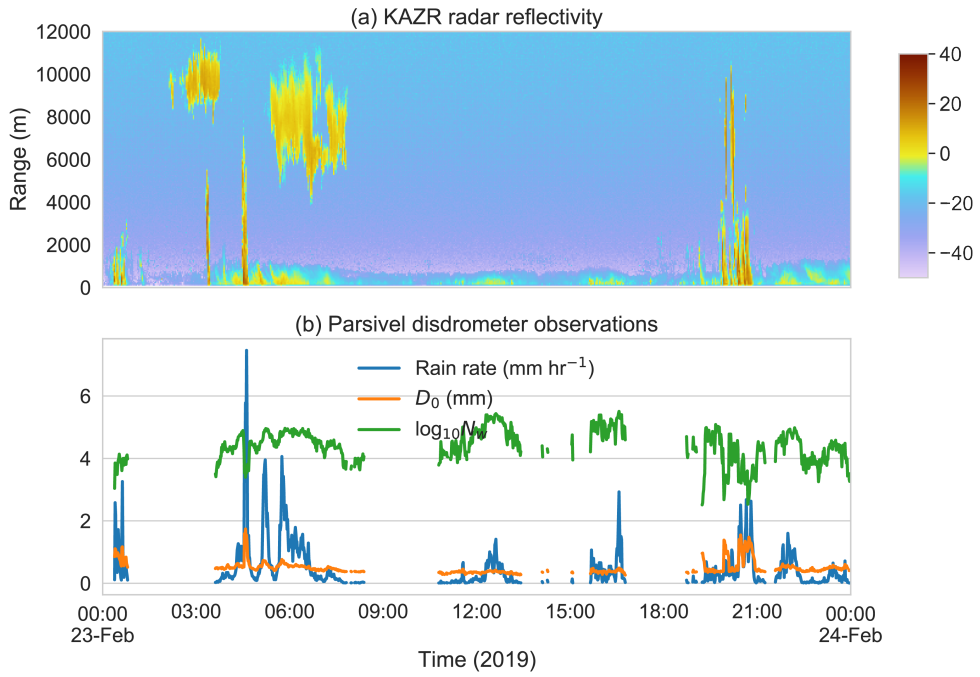

Figure 3.22: As in Figure 3.21, but for the period 0000 UTC 23 Feb - 0000 UTC 24 Feb 2019.

Table 3.3: Overview of the correlation between the width mass spectrum σ_M and the mean mass diameter D_m observed in $Lpm - Pm$ and Pm. Power-law curves give by equations from $WL14$ = Williams et al. (Williams et al., 2014); PARS = parsivel disdrometer data, and the 2DVD = two-dimensional video disdrometer data.

Site Mode	Correlation from:	σ_M vs. D_m power law curve equation
	WL4	$0.30\ {D_m}^{1.36}$
COR Lpm − Pm	PARS	$0.33\ {D_m}^{1.25}$
	2DVD	$0.32\ {D_m}^{1.40}$
SGP Lpm − Pm	PARS	$0.32\ {D_m}^{1.33}$
	2DVD	$0.33\ {D_m}^{1.27}$
MAN Lpm − Pm	PARS	$0.30\ {D_m}^{1.33}$
COR Pm	PARS	$0.35\ {D_m}^{1.15}$
	2DVD	$0.35\ {D_m}^{1.27}$
SGP Pm	PARS	$0.33\ {D_m}^{1.28}$
	2DVD	$0.35\ {D_m}^{1.20}$
MAN Pm	PARS	$0.32\ {D_m}^{1.28}$

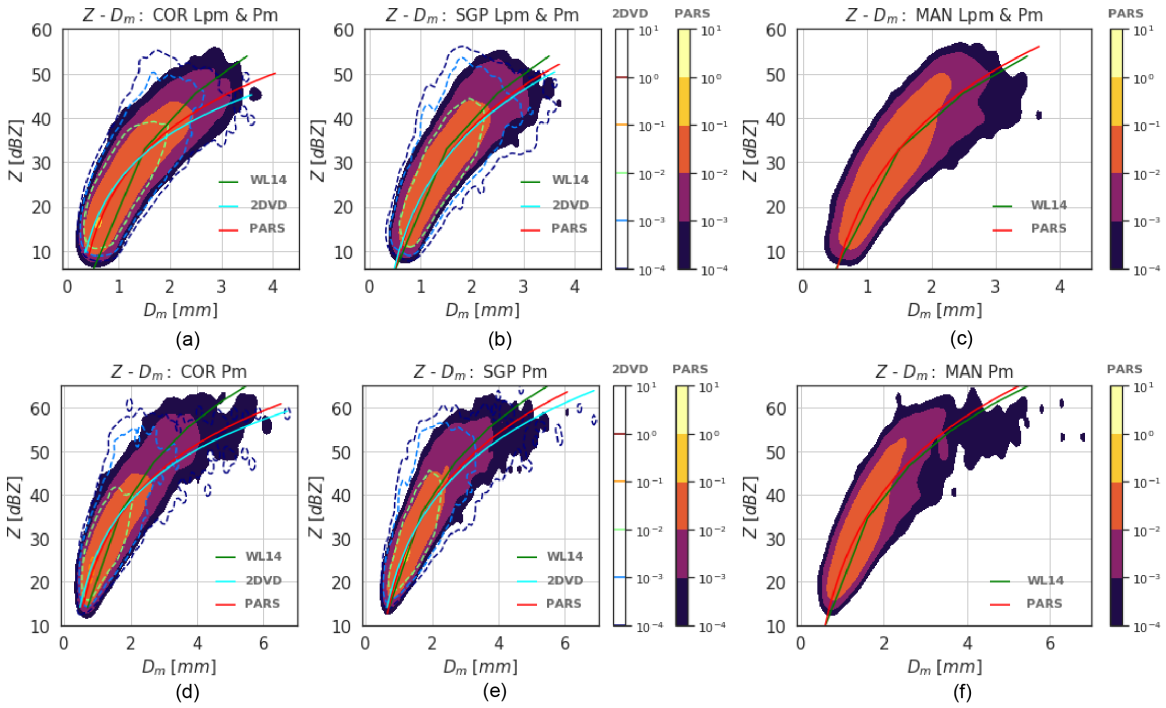

Figure 3.23: Correlation between the radar reflectivity factor Z and the mean mass diameter D_m, in the light precipitation-precipitation mode ($Lpm-Pm$ for each 1-min DSD with at least 50 drops in 5-min consecutive R ¿ 0.10 mm h^{-1}, 0.30 $< D_0 <$ 4.75 mm and $Z > 10$ dBZ) at (a) COR, (b) SGP, and (c) MAN, and in the precipitation mode (Pm for each 1-min DSD with at least 50 drops in 5-min consecutive $R >$ 0.50 mm h^{-1}, 0.50 $< D_0 <$ 9.50 mm and $Z > 10$ dBZ) at (d) COR, (e) SGP, and (f) MAN sites. DSDs indicated by color contours for the PARS and color-dashed contours for the 2DVD. Solid lines from $WL14$ (green), $PARS$ (red), and $2DVD$ (cyan) are the Z vs. D_m power-law correlation curves. DSDs = raindrop size distributions; PARS = second generation parsivel disdrometer, 2DVD = two-dimensional video disdrometer; COR = Córdoba; SGP = Southern Great Plains, and MAN = Manacapuru.

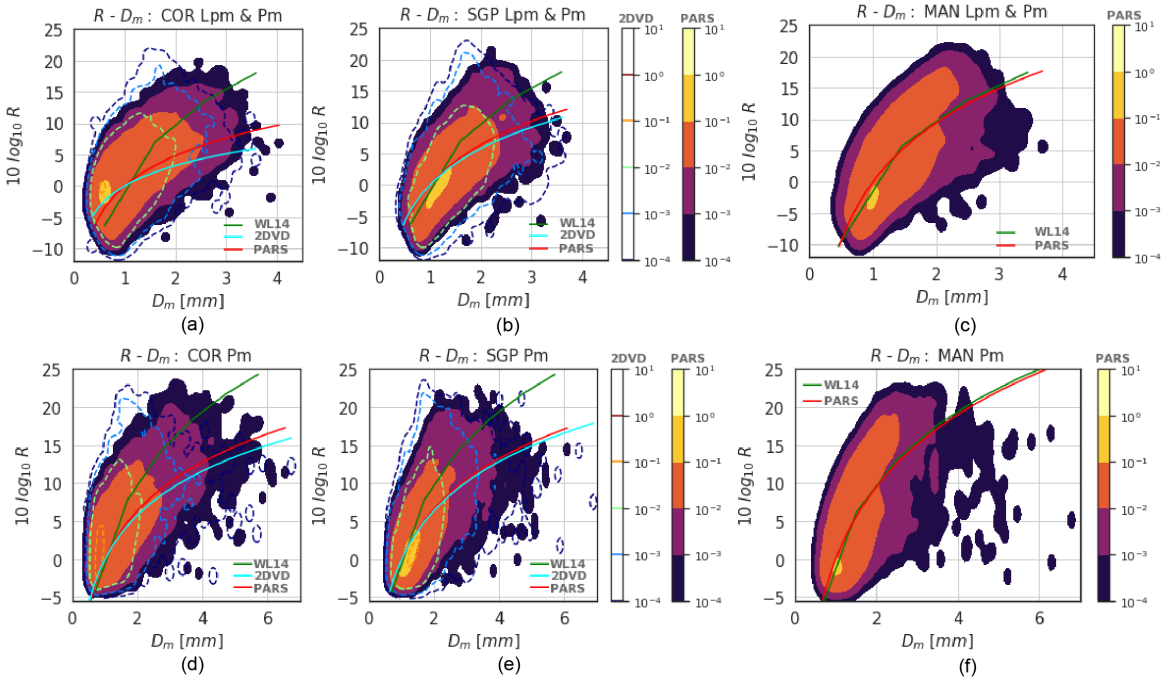

Figure 3.24: Correlation between the rain rate R as $log_{10}\ R$ and the mean mass diameter as D_m, in the light precipitation-precipitation mode ($Lpm - Pm$ for each 1-min DSD with at least 50 drops in 5-min consecutive $R > 0.10$ mm h^{-1}, $0.30 < D_0 < 4.75$ mm and $Z > 10\ dBZ$) at (a) COR, (b) SGP, and (c) MAN, and in the precipitation mode (Pm for each 1-min DSD with at least 50 drops in 5-min consecutive $R > 0.50$ mm h^{-1}, $0.50 < D_0 < 9.50$ mm and $Z > 10\ dBZ$) at (d) COR, (e) SGP, and (f) MAN sites. DSDs indicated by color contours for the PARS and color-dashed contours for the 2DVD. Solid lines from $WL14$ (green), $PARS$ (red), and $2DVD$ (cyan) are the R vs. D_m power-law correlation curves. DSDs = raindrop size distributions; PARS = second generation parsivel disdrometer, 2DVD = two-dimensional video disdrometer; COR = Córdoba; SGP = Southern Great Plains, and MAN = Manacapuru.

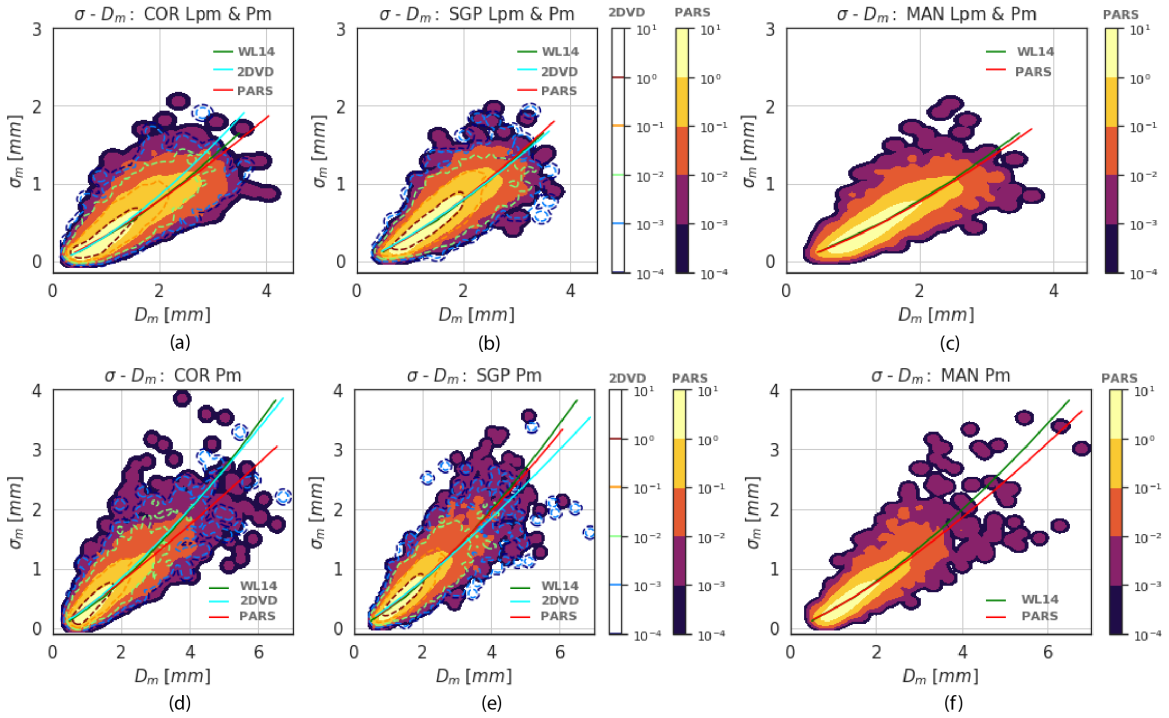

Figure 3.25: Correlation between the width mass spectrum σ_M and the mean mass diameter as D_m, in the light precipitation-precipitation mode ($Lpm - Pm$ for each 1-min DSD with at least 50 drops in 5-min consecutive $R > 0.10$ mm h^{-1}, $0.30 < D_0 < 4.75$ mm and $Z > 10$ dBZ at (a) COR, (b) SGP, and (c) MAN, and in the precipitation mode (Pm for each 1-min DSD with at least 50 drops in 5-min consecutive $R > 0.50$ mm h^{-1}, $0.50 < D_0 < 9.50$ mm and $Z > 10$ dBZ) at (d) COR, (e) SGP, and (f) MAN sites. DSDs indicated by color contours for the PARS and color-dashed contours for the 2DVD. Solid lines from $WL14$ (green), $PARS$ (red), and $2DVD$ (cyan) are the σ_M vs. D_m power-law correlation curves. DSDs = raindrop size distributions; PARS = second generation parsivel disdrometer, 2DVD = two-dimensional video disdrometer; COR = Córdoba; SGP = Southern Great Plains, and MAN = Manacapuru.

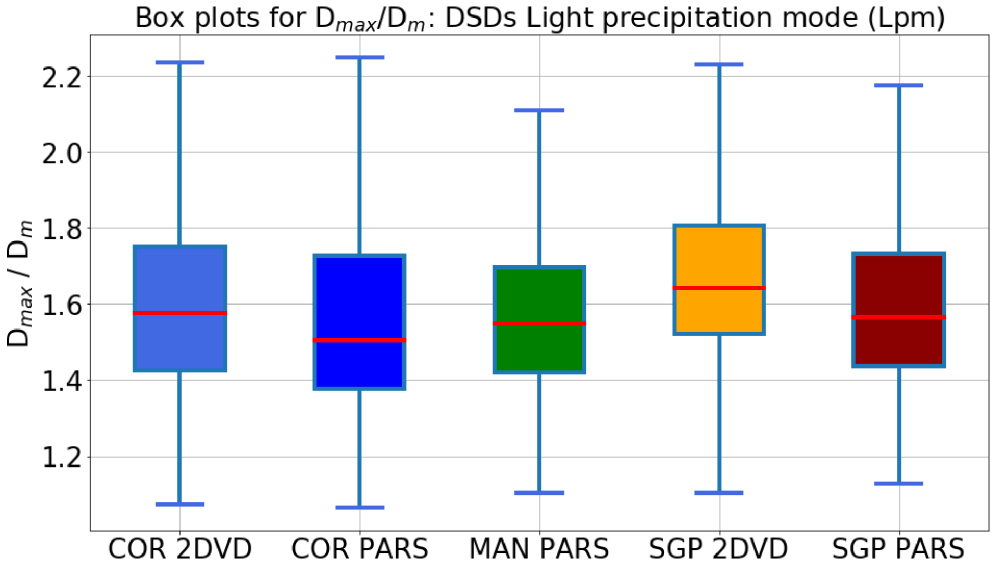

Figure 3.26: Box-and-whisker plots for the ratio of maximum raindrop diameter (D_{max}) and mass-weighted mean diameter (D_m): DSDs in the light precipitation mode (Lpm : R $<$ 0.5 mm h^{-1}) for the PARS and 2DVD at COR, SGP, and MAN sites. Tops and bottoms of boxes in blue solid line represent the 75th and 25th quartiles, respectively, and the horizontal red solid lines inside the boxes represent the median. PARS = second generation disdrometer, 2DVD = two-dimensional video disdrometer, COR = Córdoba; SGP = Southern Great Plains, and MAN = Manacapuru.

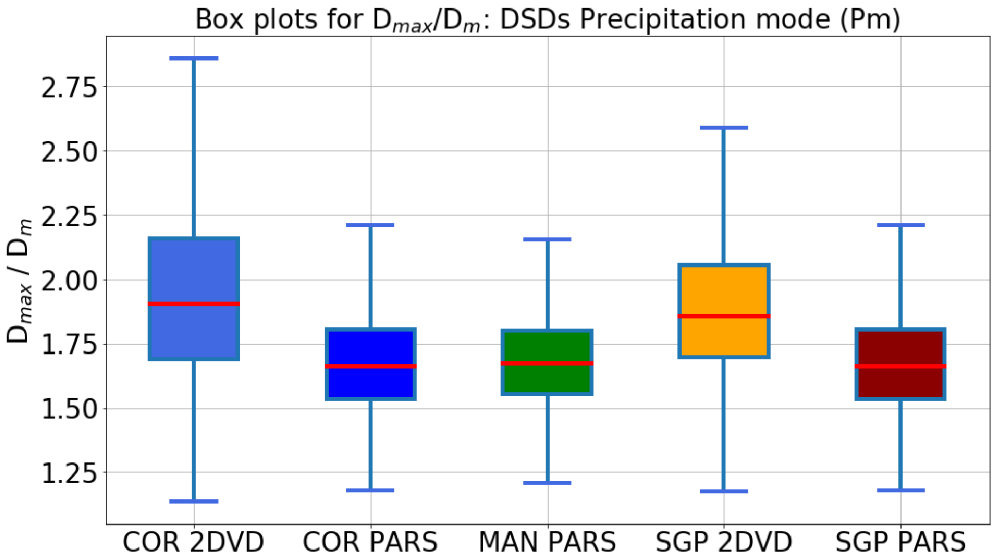

Figure 3.27: Box-and-whisker plots for the ratio of maximum raindrop diameter (D_{max}) and mass-weighted mean diameter (D_m): DSDs in the light precipitation mode (Pm : R $>$ 0.5 mm h^{-1}) for the PARS and 2DVD at COR, SGP, and MAN sites. Tops and bottoms of boxes in blue solid line represent the 75th and 25th quartiles, respectively, and the horizontal red solid lines inside the boxes represent the median. PARS = second generation disdrometer, 2DVD = two-dimensional video disdrometer, COR = Córdoba; SGP = Southern Great Plains, and MAN = Manacapuru.

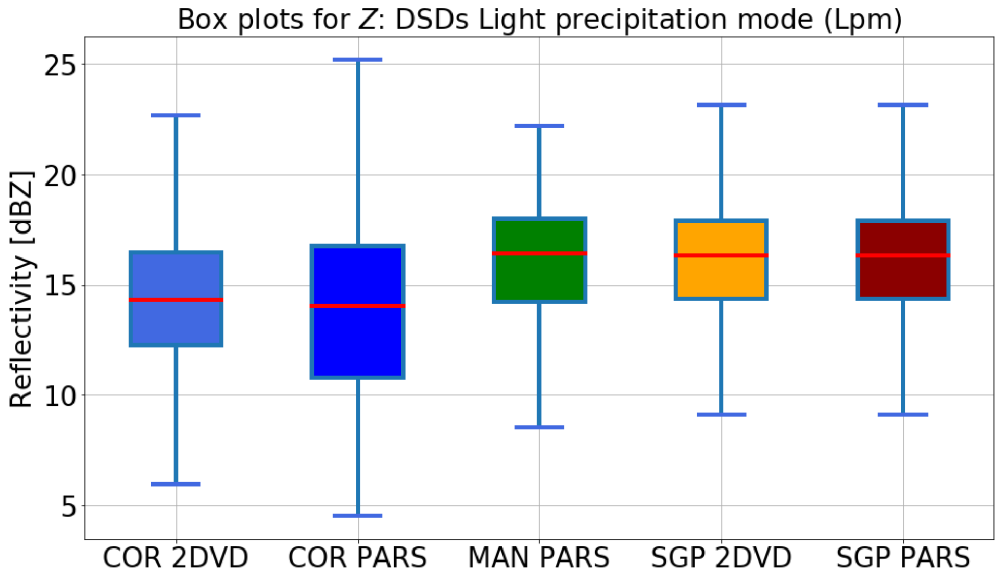

Figure 3.28: Box-and-whisker plots for the reflectivity factor (Z) in the light precipitation mode (Lpm : R < 0.5 mm h^{-1}) for the PARS and 2DVD at COR, SGP, and MAN sites. Tops and bottoms of boxes in blue solid line represent the 75th and 25th quartiles, respectively, and the horizontal red solid lines inside the boxes represent the median. PARS = second generation disdrometer, 2DVD = two-dimensional video disdrometer, COR = Córdoba; SGP = Southern Great Plains, and MAN = Manacapuru.

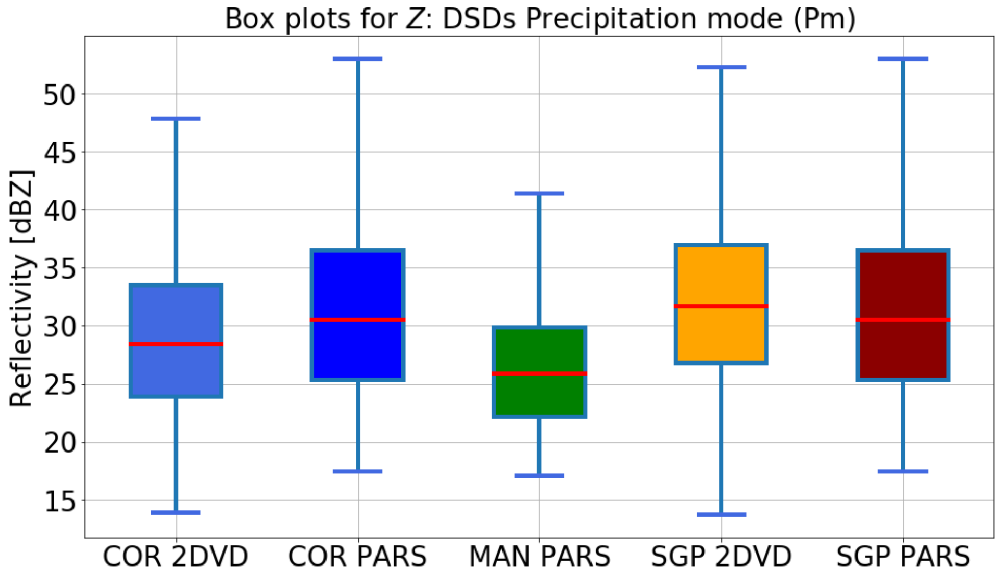

Figure 3.29: Box-and-whisker plots for the reflectivity factor (Z) in the light precipitation mode (Pm : R < 0.5 mm h^{-1}) for the PARS and 2DVD at COR, SGP, and MAN sites. Tops and bottoms of boxes in solid blue line represent the 75th and 25th quartiles, respectively, and the horizontal red solid lines inside the boxes represent the median. PARS = second generation disdrometer, 2DVD = two-dimensional video disdrometer, COR = Córdoba; SGP = Southern Great Plains, and MAN = Manacapuru.

Chapter 4

Discussion

The results presented in section 3 have evaluated a compilation of disdrometer datasets for comparisons of DSDs and the DSD parameters among three sites in the Americas. Table 4.1 provides a summary of the highest peak values in terms of pdf of the physical parameters, for DSDs classified in the light precipitation mode (Lpm) and precipitation mode (Pm), as described in section 2.

Complementing the analysis done earlier for the 3 sites (Figure 3.17), the DSD parameters for the light precipitation mode (Lpm) are restricted to $log_{10}\ N_w$ values between 3.41 and 4.70 at SGP and COR respectively and and 3.52 at MAN. The D_m values span from 0.45 and 0.90 mm in the mid-latitude sites (COR and SGP) and 0.85 mm in the tropical site (MAN). All the $N_w - D_0$ observations at the 3 sites in the Lpm are below the Bringi et al. (2009) segregation line, and thus would be categorized as stratiform, even though the radar observations we examined clearly show that this is likely precipitation formed by shallow clouds and drizzle. In addition, considering the Thompson et al. (Thompson et al., 2015) convective-stratiform segregation criteria, most of the Lpm observations would fall in the stratiform category, however less than a quarter of the N_w-D_0 observations would be classified as convective (or a region of observations that is above the corresponding segregation line).

More specifically in Lpm (Figs. 3.17-3.19), COR observations exhibited similar $log_{10}\ N_w$ high values (4.60 and 4.70 for PARS and 2DVD) to the group categorized as weak convection in Dolan et al. (2018) (4.71 for midlatitudes). However, the observed relatively smaller mean raindrop sizes ($D_0 \sim$ 0.45-0.51 mm for PARS and 2DVD), along with relatively low rain rate and liquid water content placed some Lpm observations in the group represented as vapor deposition in Dolan et al. (2018) ($D_0 \sim$ 0.68 mm for midlatitudes). Our investigation of these periods do not show ice processes being involved in the large majority of Lpm cases.

The COR site also presented a higher number of rainy minutes in all precipitation modes than the MAN site for the PARS measurements. This does not include light precipitation that may be missed by these disdrometers, including drizzle (Thurai et al., 2017). The findings of Marengo et al. (2017) showed that GoAmazon was conducted during a relatively dry period using analyses of meteorological data and model outputs for the integral observing period the campaign (from 1 January 2014 to 31 December 2015). However,

despite the surprisingly high frequency of precipitation observed in Villa Yacanto during the CACTI field campaign, it is left to future work to determine if the COR or MAN site has higher precipitation frequency climatologically.

Table 4.1: Overview of the dataset characteristics and pdf peaks from the DSD parameters observed in *Lpm* and *Pm*. Multiple peaks were determined subjectively.

Site Mode	Instrument	*No.* of rainy minutes	Peaks in 10 log_{10} R	Peaks in D_m (mm)	Peaks in log_{10} N_w
COR Lpm	PARS	20517	-5.76	0.45	4.00
					4.60
	2DVD	14295	-5.75	0.50	4.20
					4.70
SGP Lpm	PARS	8414	-5.75	0.51	3.60
				0.81	
	2DVD	16409	-5.75	0.53	3.41
				0.90	
MAN Lpm	PARS	16037	-5.77	0.85	3.52
COR Pm	PARS	10833	5.25	1.11	3.15
					3.70
	2DVD	7231	4.25	0.85	3.55
					4.20
					4.40
SGP Pm	PARS	12011	3.25	1.26	3.15
					4.40
	2DVD	10761	4.25	1.56	3.20
					4.55
MAN Pm	PARS	9821	2.75	1.25	3.60

Chapter 5

Summary and Conclusions

This study presents a comparison of the raindrop size distribution parameters variability among three deep convective regions in the Americas: the U.S. southern Great Plains and west central Argentina in the midlatitudes, and central Amazon in the tropics. Considering the lack of drop size distribution studies in South America, the ARM datasets for two types of disdrometers are analyzed here and may provide a valid reference to characterize the raindrop size spectrum in these regions that are also part of 3 major international river basins.

In order to analyze the variability of the DSD parameters at the 3 sites, the probability density functions (pdfs) of rain rate R, mass-weighted mean diameter D_m, and normalized droplet concentration N_w were presented in section 3. The DSD comparison in terms of pdfs showed that rain rates were similar between COR and SGP mid-latitude sites, which were less frequent that heavy rains at the MAN tropical site. At COR, more frequent precipitation was found with smaller median mass diameter and a broader range of normalized number concentration. This variability observed at COR was present both precipitation modes defined in this study: in a precipitation mode ($R > 0.5$ mm hr^{-1}) and a light precipitation mode ($R < 0.5$ mm hr^{-1}).

Furthermore, to examine the co-variability of the DSD parameters in each site, but also for a comparison among sites and previous drop size distribution studies, section 3 provides two-dimensional histograms of the normalized droplet concentration N_w, and the liquid water content LWC, respectively, each of these parameters versus the mean raindrop diameter D_0. Again, COR exhibits a larger variability of N_w values for both rainfall modes in comparison to SGP and MAN that extends into analysis of the $N_w - D_0$ parameter space. However, the LWC-D_0 co-variability appears to be quite similar for the sites examined in the midlatitudes (COR and SGP), contrary to the co-variability at MAN that appears to be extended towards higher values of D_0 and LWC which is a characteristic of tropical rainfall observed in previous studies, possibly related to enhanced collision-coalescence processes there (Tokay and Short, 1996; Yuter and Houze Jr, 1997; Thompson et al., 2015; Dolan et al., 2018).

The comparisons between arbitrarily-shaped DSD attributes allowed the verification of quite similar

correlations of D_m with σ_M and the reflectivity factor Z, to the power-law correlation curves found by Williams et al. (2014). Further comparison with a recent DSD global study (Gatlin et al., 2015), the median values of the D_{max}/D_m ratio are similar in the Pm, thus the Z median values are different in both modes at the 3 sites.

Surprisingly, a higher observed frequency of high N_w values in both the PARS and 2DVD distribution in Lpm and Pm, and the characteristics in Lpm appear to be a unique rain type (shallow clouds, drizzle, and light rain) that confound past works that classify precipitation types based on surface disdrometers. They resemble both the weak convection and vapor deposition features from Dolan et al. (2018) for in the $N_w - D_0$ phase space (section 4). This unique precipitation, possibly related to the location of the site in flows affected by complex terrain, will be addressed in a future study, and show the novel precipitation process observations that make the COR site unique relative to previously studied sites.

Additional analysis of aircraft-based imaging probes and the KAZR Doppler cloud radar measurements to better characterize the microphysics of rain processes in Lpm at COR may also be considered for future research.

References

Atlas, D. and Ulbrich, C. W. (1990). Early foundations of the measurement of rainfall by radar. In *Radar in Meteorology*, pages 86–97. Springer.

Baker, M. (1997). Cloud microphysics and climate. *Science*, 276(5315):1072–1078.

Barraqué, B. (2017). The common property issue in flood control through land use in f rance. *Journal of Flood Risk Management*, 10(2):182–194.

Bartholomew, M. (2014). Parsivel2 handbook. Technical report, DOE Office of Science Atmospheric Radiation Measurement (ARM) Program.

Bartholomew, M. (2017). Two-dimensional video disdrometer (vdis) instrument handbook. Technical report, DOE Office of Science Atmospheric Radiation Measurement (ARM) Program ....

Bazán, R., García, M., Lozada, J. M. D., Chalimond, M. L., Herrero, H., Bonansea, M., Bonfanti, E., Busso, F., and Cossavella, A. (2018). Estudio multidisciplinario e interinstitucional de dos fuentes principales de agua potable para la provincia de córdoba. *Revista de la Facultad de Ciencias Exactas, Físicas y Naturales*, 5:57.

Berne, A. and Krajewski, W. F. (2013). Radar for hydrology: Unfulfilled promise or unrecognized potential? *Advances in Water Resources*, 51:357–366.

Braga, R. C., Rosenfeld, D., Weigel, R., Jurkat, T., Andreae, M. O., Wendisch, M., Pöschl, U., Voigt, C., Mahnke, C., Borrmann, S., et al. (2017). Aerosol concentrations determine the height of warm rain and ice initiation in convective clouds over the amazon basin. *Atmospheric Chemistry and Physics (ACP)*, 17:14433–14456.

Bringi, V. and Chandrasekar, V. (2001). *Polarimetric Doppler weather radar: principles and applications*. Cambridge University Press.

Bringi, V., Chandrasekar, V., Hubbert, J., Gorgucci, E., Randeu, W., and Schoenhuber, M. (2003). Raindrop size distribution in different climatic regimes from disdrometer and dual-polarized radar analysis. *Journal of the atmospheric sciences*, 60(2):354–365.

Bringi, V., Williams, C., Thurai, M., and May, P. (2009). Using dual-polarized radar and dual-frequency profiler for dsd characterization: A case study from darwin, australia. *Journal of Atmospheric and Oceanic Technology*, 26(10):2107–2122.

Cancelada, M., Salio, P., Vila, D., Nesbitt, S. W., and Vidal, L. (2020). Backward adaptive brightness temperature threshold technique (bab3t): A methodology to determine extreme convective initiation regions using satellite infrared imagery. *Remote Sensing*, 12(2):337.

Caracciolo, C., Napoli, M., Porcù, F., Prodi, F., Dietrich, S., Zanchi, C., and Orlandini, S. (2012). Raindrop size distribution and soil erosion. *Journal of irrigation and drainage engineering*, 138(5):461–469.

Caracciolo, C., Porcu, F., and Prodi, F. (2008). Precipitation classification at mid-latitudes in terms of drop size distribution parameters. *Advances in Geosciences*.

Chandrasekar, V. and Bringi, V. (1987). Simulation of radar reflectivity and surface measurements of rainfall. *Journal of Atmospheric and Oceanic Technology*, 4(3):464–478.

Chase, R., Nesbitt, S., and McFarquhar, G. (2020). Evaluation of the microphysical assumptions within gpm-dpr using ground-based observations of rain and snow. *Atmosphere*, 11:619.

Chug, D. and Dominguez, F. (2019). Isolating the observed influence of vegetation variability on the climate of la plata river basin. *Journal of Climate*, 32(14):4473–4490.

Collins, P. A., Giri, F., and Williner, V. (2011). Biogeography of the freshwater decapods in the la plata basin, south america. *Journal of Crustacean Biology*, 31(1):179–191.

Deo, A. and Walsh, K. J. (2016). Contrasting tropical cyclone and non-tropical cyclone related rainfall drop size distribution at darwin, australia. *Atmospheric Research*, 181:81–94.

Dolan, B., Fuchs, B., Rutledge, S., Barnes, E., and Thompson, E. (2018). Primary modes of global drop size distributions. *Journal of the Atmospheric Sciences*, 75(5):1453–1476.

Duan, Q., Pappenberger, F., Wood, A., Cloke, H. L., and Schaake, J. (2019). *Handbook of Hydrometeorological Ensemble Forecasting*. Springer.

Emanuel, K. A. (1994). *Atmospheric convection*. Oxford University Press on Demand.

Gat, J. R. and Matsui, E. (1991). Atmospheric water balance in the amazon basin: an isotopic evapotranspiration model. *Journal of Geophysical Research: Atmospheres*, 96(D7):13179–13188.

Gatlin, P. N., Thurai, M., Bringi, V., Petersen, W., Wolff, D., Tokay, A., Carey, L., and Wingo, M. (2015). Searching for large raindrops: A global summary of two-dimensional video disdrometer observations. *Journal of Applied Meteorology and Climatology*, 54(5):1069–1089.

Giangrande, S. E., Toto, T., Jensen, M. P., Bartholomew, M. J., Feng, Z., Protat, A., Williams, C. R., Schumacher, C., and Machado, L. (2016). Convective cloud vertical velocity and mass-flux characteristics from radar wind profiler observations during goamazon2014/5. *Journal of Geophysical Research: Atmospheres*, 121(21):12–891.

Giangrande, S. E., Wang, D., Bartholomew, M. J., Jensen, M. P., Mechem, D. B., Hardin, J. C., and Wood, R. (2019). Midlatitude oceanic cloud and precipitation properties as sampled by the arm eastern north atlantic observatory. *Journal of Geophysical Research: Atmospheres*, 124(8):4741–4760.

Gong, X., Zhu, D., Zhang, L., Zhang, Y., Ge, M., Yang, W., et al. (2014). Drop size distribution of fixed spray-plate sprinklers with two-dimensional video disdrometer. *Nongye Jixie Xuebao= Transactions of the Chinese Society for Agricultural Machinery*, 45(8):128–148.

Hardin, J., Hunzinger, A., Schuman, E., Matthews, A., Bharadwaj, N., Varble, A., Johnson, K., and Giangrande, S. (2020). Cacti radar b1 processing: Corrections, calibrations, and processing report. Technical report, DOE Office of Science Atmospheric Radiation Measurement (ARM) Program.

Houze Jr, R. A., Smull, B. F., and Dodge, P. (1990). Mesoscale organization of springtime rainstorms in oklahoma. *Monthly Weather Review*, 118(3):613–654.

Jakob, C. (2003). An improved strategy for the evaluation of cloud parameterizations in gcms. *Bulletin of the American Meteorological Society*, 84(10):1387–1402.

Jakob, C. and Miller, M. (2003). Parameterization of physical processes: Clouds. *Encyclopedia of Atmospheric Sciences*, pages 1692–1698.

Joss, J., Waldvogel, A., and Collier, C. (1990). Precipitation measurement and hydrology. In *Radar in meteorology*, pages 577–606. Springer.

Karl, T. R. and Knight, R. W. (1998). Secular trends of precipitation amount, frequency, and intensity in the united states. *Bulletin of the American Meteorological society*, 79(2):231–242.

Krajewski, W. and Smith, J. A. (2002). Radar hydrology: rainfall estimation. *Advances in water resources*, 25(8-12):1387–1394.

Lloyd, G., Dearden, C., Choularton, T., Crosier, J., and Bower, K. (2014). Observations of the origin and distribution of ice in cold, warm, and occluded frontal systems during the diamet campaign. *Monthly Weather Review*, 142(11):4230–4255.

Löffler-Mang, M. and Joss, J. (2000). An optical disdrometer for measuring size and velocity of hydrometeors. *Journal of Atmospheric and Oceanic Technology*, 17(2):130–139.

Lozada, J. M. D., García, C. M., Herrero, H., Barchiesi, G. M., Romagnoli, M., Portapila, M., Lopez, F., Castelló, E., Cossavella, A., and Brarda, J. P. (2015). Cuantificación del escurrimiento superficial de la cuenca del río carcarañá. *Revista de la Facultad de Ciencias Exactas, Físicas y Naturales*, 2(1):59–72.

Marengo, J. A., Fisch, G. F., Alves, L. M., Sousa, N. V., Fu, R., and Zhuang, Y. (2017). Meteorological context of the onset and end of the rainy season in central amazonia during the goamazon2014/5. *Atmospheric Chemistry and Physics*, 17(12):7671.

Marshall, J. S. and Palmer, W. M. K. (1948). The distribution of raindrops with size. *Journal of meteorology*, 5(4):165–166.

Martin, S., Artaxo, P., Machado, L., Manzi, A., Souza, R., Schumacher, C., Wang, J., Andreae, M., Barbosa, H., Fan, J., et al. (2016a). Introduction: observations and modeling of the green ocean amazon (goamazon2014/5). *Atmospheric Chemistry and Physics*, 16(8).

Martin, S., Mei, F., Alexander, L., Artaxo, P., Barbosa, H., Bartholomew, M. J., Biscaro, T., Buseck, P., Chand, D., Comstock, J., et al. (2016b). Campaign datasets for observations and modeling of the green ocean amazon (goamazon). Technical report, Atmospheric Radiation Measurement (ARM) Archive, Oak Ridge National ....

Martins, R. C., Machado, L. A., and Costa, A. A. (2010). Characterization of the microphysics of precipitation over amazon region using radar and disdrometer data. *Atmospheric Research*, 96(2-3):388–394.

Mulholland, J. P., Nesbitt, S. W., and Trapp, R. J. (2019). A case study of terrain influences on upscale convective growth of a supercell. *Monthly Weather Review*, 147(12):4305–4324.

Mulholland, J. P., Nesbitt, S. W., Trapp, R. J., Rasmussen, K. L., and Salio, P. V. (2018). Convective storm life cycle and environments near the sierras de córdoba, argentina. *Monthly Weather Review*, 146(8):2541–2557.

Nesbitt, S. and coauthors (2016). Experimental design overview document, relampago. Technical report.

Nesbitt, S. W., Cifelli, R., and Rutledge, S. A. (2006). Storm morphology and rainfall characteristics of trmm precipitation features. *Monthly Weather Review*, 134(10):2702–2721.

Nesbitt, S. W., Zipser, E. J., and Cecil, D. J. (2000). A census of precipitation features in the tropics using trmm: Radar, ice scattering, and lightning observations. *Journal of Climate*, 13(23):4087–4106.

Nobre, C. A. (1984). The amazon and climate. Technical report, NASA Center for Aerospace Information (CASI).

Nunes, A. M., Silva Dias, M. A., Anselmo, E. M., and Morales, C. A. (2016a). Severe convection features in the amazon basin: a trmm-based 15-year evaluation. *Frontiers in Earth Science*, 4:37.

Nunes, A. M. P., Silva Dias, M. A. F., Anselmo, E. M., and Morales, C. A. (2016b). Severe convection features in the amazon basin: A trmm-based 15-year evaluation. *Frontiers in Earth Science*, 4:37.

Pal, S., Dominguez, F., Gochis, D. J., and Demaria, E. (2019). Hydroclimatological modeling of the carcarañá river basin in argentina. In *99th American Meteorological Society Annual Meeting*. AMS.

Paukert, M., Fan, J., Rasch, P. J., Morrison, H., Milbrandt, J., Shpund, J., and Khain, A. (2019). Three-moment representation of rain in a bulk microphysics model. *Journal of Advances in Modeling Earth Systems*, 11(1):257–277.

Penide, G., Kumar, V. V., Protat, A., and May, P. T. (2013). Statistics of drop size distribution parameters and rain rates for stratiform and convective precipitation during the north australian wet season. *Monthly weather review*, 141(9):3222–3237.

Rasmussen, K. L., Chaplin, M., Zuluaga, M., and Houze Jr, R. (2016). Contribution of extreme convective storms to rainfall in south america. *Journal of Hydrometeorology*, 17(1):353–367.

Rasmussen, K. L. and Houze Jr, R. A. (2011). Orogenic convection in subtropical south america as seen by the trmm satellite. *Monthly Weather Review*, 139(8):2399–2420.

Rasmussen, K. L., Zuluaga, M. D., and Houze Jr, R. A. (2014). Severe convection and lightning in subtropical south america. *Geophysical Research Letters*, 41(20):7359–7366.

Rauber, R. M. and Nesbitt, S. L. (2018). *Radar Meteorology: A First Course*. John Wiley & Sons.

Romatschke, U. and Houze Jr, R. A. (2010). Extreme summer convection in south america. *Journal of Climate*, 23(14):3761–3791.

Rosenfeld, D. and Ulbrich, C. W. (2003). Cloud microphysical properties, processes, and rainfall estimation opportunities. In *Radar and Atmospheric Science: A Collection of Essays in Honor of David Atlas*, pages 237–258. Springer.

Rosewell, C. J. (1986). Rainfall kinetic energy in eastern australia. *Journal of Climate and Applied Meteorology*, 25(11):1695–1701.

Rutledge, S. A., Houze, Robert A., J., Biggerstaff, M. I., and Matejka, T. (1988). The Oklahoma–Kansas Mesoscale Convective System of 10–11 June 1985: Precipitation Structure and Single-Doppler Radar Analysis. *Monthly Weather Review*, 116(7):1409–1430.

Schumacher, C. (2016). Observations and modeling of the green ocean amazon 2014/15: Parsivel2 field campaign report. Technical report, DOE Office of Science Atmospheric Radiation Measurement (ARM) Program ....

Seliga, T. A. and Bringi, V. (1976). Potential use of radar differential reflectivity measurements at orthogonal polarizations for measuring precipitation. *Journal of Applied Meteorology*, 15(1):69–76.

Stenta, H., Riccardi, G., and Basile, P. A. (2016). Modelación distribuida del escurrimiento superficial en la cuenca del río tercero-carcaraña. *Aqua-LAC*.

Sui, C.-H., Tsay, C.-T., and Li, X. (2007). Convective–stratiform rainfall separation by cloud content. *Journal of Geophysical Research: Atmospheres*, 112(D14).

Testud, J., Oury, S., Black, R. A., Amayenc, P., and Dou, X. (2001). The concept of "normalized" distribution to describe raindrop spectra: A tool for cloud physics and cloud remote sensing. *Journal of Applied Meteorology*, 40(6):1118–1140.

Thompson, E. J., Rutledge, S. A., Dolan, B., and Thurai, M. (2015). Drop size distributions and radar observations of convective and stratiform rain over the equatorial indian and west pacific oceans. *Journal of the Atmospheric Sciences*, 72(11):4091–4125.

Thurai, M. and Bringi, V. (2008). Rain microstructure from polarimetric radar and advanced disdrometers. In *Precipitation: Advances in Measurement, Estimation and Prediction*, pages 233–284. Springer.

Thurai, M., Bringi, V., and May, P. (2010). Cpol radar-derived drop size distribution statistics of stratiform and convective rain for two regimes in darwin, australia. *Journal of Atmospheric and Oceanic Technology*, 27(5):932–942.

Thurai, M., Bringi, V., and Petersen, W. (2009). Rain microstructure retrievals using 2-d video disdrometer and c-band polarimetric radar. *Advances in geosciences*, 20.

Thurai, M., Gatlin, P., Bringi, V., Petersen, W., Kennedy, P., Notaroš, B., and Carey, L. (2017). Toward completing the raindrop size spectrum: Case studies involving 2d-video disdrometer, droplet spectrometer, and polarimetric radar measurements. *Journal of Applied Meteorology and Climatology*, 56(4):877–896.

Thurai, M., Huang, G., Bringi, V., Randeu, W., and Schönhuber, M. (2007). Drop shapes, model comparisons, and calculations of polarimetric radar parameters in rain. *Journal of atmospheric and oceanic technology*, 24(6):1019–1032.

Thurai, M., Petersen, W., Tokay, A., Schultz, C., and Gatlin, P. (2011). Drop size distribution comparisons between parsivel and 2-d video disdrometers. *Advances in Geosciences*, 30.

Tokay, A., Kruger, A., Krajewski, W. F., Kucera, P. A., and Pereira Filho, A. J. (2002). Measurements of drop size distribution in the southwestern amazon basin. *Journal of Geophysical Research: Atmospheres*, 107(D20):LBA–19.

Tokay, A., Petersen, W. A., Gatlin, P., and Wingo, M. (2013). Comparison of raindrop size distribution measurements by collocated disdrometers. *Journal of Atmospheric and Oceanic Technology*, 30(8):1672–1690.

Tokay, A. and Short, D. A. (1996). Evidence from tropical raindrop spectra of the origin of rain from stratiform versus convective clouds. *Journal of applied meteorology*, 35(3):355–371.

Tokay, A., Wolff, D. B., and Petersen, W. A. (2014). Evaluation of the new version of the laser-optical disdrometer, ott parsivel2. *Journal of Atmospheric and Oceanic Technology*, 31(6):1276–1288.

Uijlenhoet, R. and Pomeroy, J. (2001). Raindrop size distributions and radar reflectivity-rain rate relationships for radar hydrology. *Hydrology and Earth System Sciences*, pages 615–627.

Ulbrich, C. W. (1983). Natural variations in the analytical form of the raindrop size distribution. *Journal of climate and applied meteorology*, 22(10):1764–1775.

Ulbrich, C. W. and Atlas, D. (1978). The rain parameter diagram: Methods and applications. *Journal of Geophysical Research: Oceans*, 83(C3):1319–1325.

Valverde, M. C. and Marengo, J. A. (2014). Extreme rainfall indices in the hydrographic basins of brazil. *Open Journal of Modern Hydrology*, 2014.

Varble, A., Hardin, J. C., Bharadwaj, N., Feng, Z., Marquis, J., Nesbitt, S. W., and Zhang, Z. (2019a). Sensitivity of deep convective upscale growth to precipitation properties and ambient environmental conditions during the cacti field campaign. *AGUFM*, 2019:A53U–3042.

Varble, A., Nesbitt, S., Salio, P., Avila, E., Borque, P., DeMott, P., McFarquhar, G., van den Heever, S., Zipser, E., Gochis, D., et al. (2019b). Cloud, aerosol, and complex terrain interactions (cacti) field campaign report. Technical report, ARM Data Center, Oak Ridge National Laboratory (ORNL), Oak Ridge, TN (United States).

Vaughan, G., Methven, J., Anderson, D., Antonescu, B., Baker, L., Baker, T., Ballard, S., Bower, K., Brown, P., Chagnon, J., et al. (2015). Cloud banding and winds in intense european cyclones: Results from the diamet project. *Bulletin of the American Meteorological Society*, 96(2):249–265.

Wang, D., Giangrande, S. E., Bartholomew, M. J., Hardin, J., Feng, Z., Thalman, R., and Machado, L. A. (2018). The green ocean: precipitation insights from the goamazon2014/5 experiment. *Atmospheric Chemistry and Physics Discussions (Online)*, 18(BNL-205773-2018-JAAM).

Williams, C. R., Bringi, V., Carey, L. D., Chandrasekar, V., Gatlin, P. N., Haddad, Z. S., Meneghini, R., Joseph Munchak, S., Nesbitt, S. W., Petersen, W. A., et al. (2014). Describing the shape of raindrop size distributions using uncorrelated raindrop mass spectrum parameters. *Journal of Applied Meteorology and Climatology*, 53(5):1282–1296.

Williams, E., Rosenfeld, D., Madden, N., Gerlach, J., Gears, N., Atkinson, L., Dunnemann, N., Frostrom, G., Antonio, M., Biazon, B., Camargo, R., Franca, H., Gomes, A., Lima, M., Machado, R., Manhaes, S., Nachtigall, L., Piva, H., Quintiliano, W., Machado, L., Artaxo, P., Roberts, G., Renno, N., Blakeslee, R., Bailey, J., Boccippio, D., Betts, A., Wolff, D., Roy, B., Halverson, J., Rickenbach, T., Fuentes, J., and Avelino, E. (2002). Contrasting convective regimes over the amazon: Implications for cloud electrification. *Journal of Geophysical Research: Atmospheres*, 107(D20):LBA 50–1–LBA 50–19.

Williams, E. R. (1995). Meteorological aspects of thunderstorms. *Handbook of Atmospheric Electrodynamics*, 1:27–60.

Willis, P. T. (1984). Functional fits to some observed drop size distributions and parameterization of rain. *Journal of the atmospheric sciences*, 41(9):1648–1661.

Wilson, J. W. and Brandes, E. A. (1979). Radar measurement of rainfall—a summary. *Bulletin of the American Meteorological Society*, 60(9):1048–1060.

Wolf, A. T., Natharius, J. A., Danielson, J. J., Ward, B. S., and Pender, J. K. (1999). International river basins of the world. *International Journal of Water Resources Development*, 15(4):387–427.

Yuter, S. E. and Houze Jr, R. A. (1997). Measurements of raindrop size distributions over the pacific warm pool and implications for z–r relations. *Journal of Applied Meteorology*, 36(7):847–867.

Zipser, E. J., Cecil, D. J., Liu, C., Nesbitt, S. W., and Yorty, D. P. (2006). Where are the most intense thunderstorms on earth? *Bulletin of the American Meteorological Society*, 87(8):1057–1072.